

MCG4151 - Design of Artificial Joint Prosthetics
Final Report
Hip Prosthesis
Group #5

Ana Brennan (8157246) Michael Botros (8327615)
Rachel Cohen (8076627) Hunter Marriott (8258832)
Allison Tolgyesi (8127047)

December 2, 2019

Contents

1	Introduction	1
2	Anatomy of the Hip	2
2.1	Skeletal System	2
2.2	Musculature	3
3	Pathology of the Hip	4
3.1	Arthritis	4
3.2	Osteoporosis	4
3.3	Osteonecrosis	5
4	Hip Replacement Surgery	5
5	Critical Review of Current Hip Prostheses	7
5.1	Components	7
5.2	Geometry	7
5.2.1	Femoral Stem	7
5.2.2	Femoral head	8
5.2.3	Acetabular Shell and Liner	9
5.3	Causes of Hip Implant Failure	11
5.4	Modular vs. Non-modular Hip Implants	11
5.5	Review of an Optimized Hip Prosthesis	13
5.6	Fixation Techniques	15
6	Materials Used in Implants	15
7	Gait Analysis	17
7.1	Normal Gait	17
7.2	Ground Reaction Forces	18

7.3	Hip Kinematics	19
7.4	Hip Contact Forces	21
8	Structural and Functional Analysis of the Hip	24
8.1	Structural Analysis of the Natural Hip	24
8.2	Functional Analysis of the Natural Hip	26
9	Stability of the Hip Joint	28
10	Structural and Functional Design Specifications	29
11	Static Force Analysis of Biological Joint	30
11.1	Joint Reaction Forces	30
11.2	Loading Response	30
11.3	Toe Off	32
12	Dynamic Force Analysis of Biological Joint	33
12.1	Foot Analysis	33
12.2	Shank Analysis	35
12.3	Thigh Analysis	37
12.4	Dynamic Joint Reactions	38
13	Chosen Device	39
13.1	Device Components	42
13.2	Material Selection	44
13.3	Design Originality	46
13.4	Device Range of Motion	48
14	Stress Analysis	50
14.1	Analysis of the biological joint	50
14.2	Analysis of the Bone and Implant	51
14.3	Stress Shielding	55

14.4 Contact Stresses	55
14.5 Wear Analysis of the Acetabular Liner	56
14.6 Fatigue Analysis of Femoral Stem	56
15 Testing and Evaluation Methods	58
16 Conclusion	59
Appendices	74
A Anthropometric Data	74
A.1 Winter's Anthropometric Data	74
A.2 Elderly Anthropometric Data	75
B Static Force Calculations	77
C Inverse Dynamics Variable Definitions	81
D Stress Calculations	83
D.1 Hertz Theory	88
E Muscle Force Angle and Location	89

List of Figures

1	Main components of an artificial hip joint	7
2	Constricted hip ROM with smaller head size (left) and larger hip ROM with larger head size (right)	8
3	Three types of polyethylene liner designs: Type A (inner chamfer), Type B (bevel), Type C (straight)	9
4	Acetabular liner with relevant measurements for hip stability	10
5	Modular fluted titanium stems	12
6	Range of motion of a standard cup (left) and a modular dual mobility cup (right).	12
7	Hip implant model for dynamic finite element analysis	13
8	Walking Gait Cycle.	18
9	Hip kinematics through the gait cycle.	20
10	Hip kinematics differences between healthy subjects and THA patients. .	21
11	Resultant hip contact forces on an implant for (a) walking and (b) stair climbing	22
12	Free body diagram of the hip joint	25
13	Ground Reaction Forces in the x-, y-, and z-directions	31
14	Free body diagram of the foot and ankle in the sagittal (left) and frontal (right) planes	34
15	Free body diagram of the shank in the frontal (left) and sagittal (right) planes	36
16	Free body diagrams of the thigh in the sagittal (left) and frontal (right) planes	37
17	Hip contact angles throughout the gait cycle	38
18	Hip contact forces throughout the gait cycle	39

19	Hip implant design - isometric view on the left, and exploded view on the right (shown in order: acetabular shell, acetabular liner, femoral head and femoral stem)	40
20	Projected views and render of the acetabular shell (dimensions in mm) . .	43
21	Projected views and render of the acetabular liner (dimensions in mm) . .	43
22	Projected views and render of the femoral head (dimensions in mm) . . .	44
23	Projected views and render of the femoral stem (dimensions in mm) . . .	44
24	Locations of the femur that are most likely to have osteolysis when the implant is placed	47
25	Sagittal plane range of motion of the designed hip implant: 100° flexion and 50° extension	48
26	Frontal plane range of motion of the designed hip implant: 51° adduction and 60° abduction	49
27	Transverse plane range of motion of the designed hip implant: 121.23° internal rotation and 67.67° external rotation	49
28	Bone forces and eccentricity	50
29	Sections of the prosthetic for stress analysis	51
30	a) The implant cross section dimensions b) The entire cross section at section C-C	53
31	Free body diagram for stress analysis at section C-C	53
32	Modified Goodman fatigue diagram for four cross-sections of the femoral stem	58
A.33	Classical anthropometric model from Drillis and Contini, 1964 - via Winter, 2009	74
E.34	Muscle and femoral head angles	89
E.35	Moment arm and muscle attachment dimensions	90
E.36	Location and angle of the muscle at loading response	91

List of Tables

1	Parameters to measure liner geometry	9
2	Femoral head and acetabular cup dimensions (mm) simulated by Shaik et al.	14
3	Femoral stem dimensions simulated by Shaik et al	14
4	Advantages and Disadvantages of various material combinations for bearing surfaces	17
5	Estimated natural hip PROM and AROM (both in degrees) in healthy adults	27
6	Estimated post-operative bilateral artificial hip PROM (in degrees)	27
7	Limb angles and GRF at loading response	31
8	Static forces at the hip, knee and ankle joints at 18% gait	32
9	Limb angles and GRF at toe off	32
10	Static forces at the hip, knee and ankle joints at 52% gait	33
11	Dynamic forces at the hip, knee and ankle joints at 52% gait	39
12	Prosthesis ROM compared to ROM values relevant to the elderly female user (units in degrees)	50
13	Stress Analysis for the natural bone implant at 3 cross sections	51
14	General geometrical variables used in the stress analysis 29	52
15	Stresses in the implant for all cross sections from Figure 29	54
16	Stresses in the bone for all cross sections from Figure 29	54
17	Stresses in the cement for all cross sections found in Figure 29	54
18	Cross-sectional areas and stresses in femoral stem	58
A19	Variable names and values used in foot inverse dynamics analysis at 52% gait	81
A20	Variable names and values used in shank inverse dynamics analysis at 52% gait	82

A21 Variable names and values used in thigh inverse dynamics analysis at 52% gait	82
A22 Material Properties for Hertz Analysis	88

1 Introduction

Total hip replacements, also known as total hip arthroplasties (THA), are a procedure in which the femoral head, femoral neck and acetabular cup are replaced in a damaged hip. Primary causes of a damaged hip requiring a THA include arthritis (rheumatoid and osteoarthritis), hip dysplasia, avascular necrosis, and hip fracture [1].

The components of the THA include the femoral stem, which is anchored into the femur, the femoral head, the acetabular cup and the cup liner. These components can be made from a variety of materials, including titanium alloys, cobalt-chromium alloys, ceramic, and various polymers. Bearing materials can also vary from metal-on-metal (MoM), metal-on-polymer (MoP), ceramic-on-ceramic (CoC) and more; all with their own advantages and disadvantages. Design considerations for each component must allow the implant to be able to withstand loading from day-to-day tasks for upwards of 15 years.

The following report details the design of a THA implant specifically for a 70 year old female who is 65.3kg and 1.56m tall. The implant consists of a Co-Cr-Mo head, a Ti-6Al-7Nb stem, neck, and acetabular cup, and a cup liner made of crossed linked polyethylene (XLPE). Static and dynamic force analyses were performed during peak loading times during gait and the corresponding stresses felt by the implant and natural bone were analyzed. Fatigue and wear analyses were performed to determine the lifetime of the implant. It was found that this implant will be able to withstand a lifetime of at least 10 years without failure. A critical analysis of current commercial implants is performed and the ingenuity of the proposed implant design is discussed.

2 Anatomy of the Hip

2.1 Skeletal System

The hip joint is a synovial ball-and-socket joint and is one of the body's largest weight-bearing joints. The hip is composed of two parts: the femoral head, which is a ball-shaped piece of bone that is located at the proximal end of the femur, and the acetabulum, which is a deep socket in the pelvis into which the femoral head fits [2]. The pelvic girdle connects the lower limbs to the axial skeleton and transfers the weight from the upper body to the lower limbs. The pelvic girdle is composed of the sacrum and two pelvic bones, called the os coxae [3]. The adult pelvis is composed of three regions: the ilium, ischium and pubis [3]. These three regions all join at the acetabulum on the pelvis [3].

The hip joint is a diarthrotic joint that allows for multiaxial movement including extension, flexion, abduction, adduction, circumduction and rotation of the thigh [3]. The deep socket of the hip joint allows for maximal stability. The acetabulum socket is deepened by a ring of fibrocartilage called the acetabular labrum [3]. The labrum's diameter is less than the head of the femur, which makes for a tight fit.

There are significant structural differences between the male and female pelvis. The female pelvis is tilted forward, is more shallow, has a broader true pelvis, has a wider pubic angle, is made of bone that is smoother, lighter and less dense, and has smaller acetabula that are spaced farther apart. The male pelvis is less tilted forward, has a true pelvis that is narrow and deep, has a more acute pubic angle, is made of bone that is heavier with more prominent markings, and has larger acetabula that are spaced closer together [3].

The femur is the longest, largest, and strongest bone in the body [3]. The femur articulates with the hip joint proximally, then crosses medially to articulate with the knee joint. The angle that the femur makes as it articulates with the knee is called the Q-angle. This configuration allows the knee joints to be medially closer to the centre

of mass (COM), which increases balance [3]. The head of the femur is attached to the shaft by the neck. The neck extends laterally from the pelvis and is the weakest part of the femur. When the neck of the femur is fractured, this is commonly known as a broken hip [3]. The lateral greater trochanter and the posteromedial lesser trochanter are projections at the junction of the shaft and neck [3]. These projections are muscle attachment sites for the hip and buttock muscles.

2.2 Musculature

Several strong ligaments reinforce the hip joint. These are the iliofemoral ligament, which is a strong V-shaped ligament anteriorly, the pubofemoral ligament, a triangular thickening of the inferior part of the capsule, and the ischiofemoral ligament, a spiraling posterior ligament [3]. The ligaments are arranged such that they “screw” the femoral head into the acetabulum when a person stands up straight, providing more stability [3]. The ligamentum teres is a flat intracapsular ligament that connects the head of the femur to the inner lip of the acetabulum. It is slack during most hip movements and does not contribute to hip stability [3]. It does contain an artery that helps to supply the head of the femur. Damage to this artery can lead to severe arthritis of the hip joint [3].

The hip is surrounded by large muscles that support the joint and allow a large range of motion (ROM) [2]. These muscle groups include the gluteals, adductors, iliopsoas, quadriceps and hamstrings.

The gluteals act to extend, abduct, and medially rotate the thigh [3]. The adductors muscle group adduct, flex and medially rotate the thigh [3]. The iliopsoas muscle group flexes the thigh [3]. While the quadriceps muscle mostly provides stability for the knee, it also acts to flex the thigh. The hamstring acts to extend the thigh and medially or laterally rotate the thigh [3].

Major nerves and blood vessels also run through the hip. These include the sciatic nerve at the back of the hip and femoral nerve at the front of the hip, and the femoral artery, which begins in the pelvis and passes by the front of the hip and down the thigh [3].

3 Pathology of the Hip

3.1 Arthritis

Osteoarthritis (OA) is a degenerative joint disease and is the most common type of arthritis [4,5]. It is the leading cause of total hip arthroplasty (THA) [6]. OA is generally described as “wear-and-tear arthritis” [3], however, it has been found that there may also be an inflammatory component [7, 8]. Cartilage damaged through everyday activity is typically replaced in a healthy individual, however that damage is minimal [3]. Those suffering from OA have cartilage damage occurring at a faster pace than the body can regenerate it [3]. OA is distinguished by two important structural changes [9–11]: first is a loss of cartilage, and second is hypertrophy of bone or the formation of bony deposits on the margins, known as osteophytes [9, 10, 12]. Cartilage damage is thought to be due to repetitive compression and abrasion of the joint surfaces, which leads to excessive release of cartilage-destroying enzymes, causing it to soften and erode [3, 12]. Primary OA, the most common kind of OA and has no known cause but is mainly present in elderly people [9, 12, 13]. Primary OA generally presents little issue with flat ground gait, however stairs and slopes can become difficult and painful [9]. Secondary OA typically occurs at a younger age and can be caused by metabolic conditions leading to substance buildup in joints, anatomical factors, serious injury or inflammatory disorders [12, 13]. Prevalence of OA has been shown to increase with age [4, 9, 12, 14–16], however, there exist other risk factors for the disease. Sex is a strong predictor of OA [17], as women can be up to twice as likely as men to develop the disease [12, 18]. Obesity [19, 20] and traumatic joint injury are also factors [14].

3.2 Osteoporosis

A common cause for requiring THA is a fracture of the femur bone on or near the femoral neck [21]. Fracture can be caused by traumatic injuries, however as an individual ages, the risk of hip fracture rises with the occurrence of osteoporosis [22]. Osteoporosis is

a skeletal disorder characterized by low bone mass and deterioration of the bone that most commonly affects the hip and lumbar vertebrae [22,23]. The World Health Organization defines osteoporosis as a bone mineral density below 2.5 standard deviations of the mean of young women [24]. Osteoporosis accounts for up to 51% of fractures in women and 24% in men resulting in 250,000 osteoporotic hip fractures annually in the USA [25,26]. Not only is osteoporosis a reason for requiring a THA, it also presents complications with the implants post-surgery. The reduced bone regeneration capacity and the lower bone density results in a decreased pull-out strength of implants [27].

3.3 Osteonecrosis

Osteonecrosis is estimated to affect between 20,000 to 30,000 newly diagnosed patients each year in the USA and accounts for roughly 10% of all THAs performed in the USA [28,28,29]. Osteonecrosis is a loss of integrity of subchondral bone structure due to a loss of microcirculation [30]. This abnormal circulation leads to necrosis of the bone, causing it to collapse [30]. It most commonly affects the proximal end of the femur [28]. The disease can be caused by traumatic events such as femoral neck fractures or direct injury of bone marrow elements causing damage to the extraosseous blood vessels [28,31]. This disrupts blood supply in the affected region, causing the tissue to die. Atraumatic causes include prolonged use of corticosteroids, alcohol abuse, and those who have suffered from leukemia and lymphoma [32–35].

4 Hip Replacement Surgery

Hips that are severely damaged by arthritis, trauma, necrosis or childhood diseases generally tend to need a THA [36,37]. The first THA was performed in 1962, although partial hip replacements have been occurring since the 1920's [36,38].

To perform the surgery, the patient is either supine or on their side [38]. The surgeon makes an incision of 10-12cm through the anterior, posterior or side of the body, separating the muscles in the area, dividing the joint capsule and exposing the joint [36,38].

Following the incision, the leg is rotated to dislocate the femur head from the acetabulum [36–38]. A bone saw is used to cut the neck of the femur either before or after it is dislocated [36,38]. At this point, soft tissue, known as the labrum, is removed around the rim of the socket as well as the joint cartilage and power driven reamers remove some bone from the acetabulum to make room for the implant [36,38]. The acetabular component secures into the acetabulum either through a tight fit or with two screws into the pelvis bone [36,38]. Next, a polyethylene liner fits into the metal shell [38]. The surgeon then mixes the bone cement if the press fit method is not being used. The bone cement is created by mixing a liquid monomer called MMA with a PMMA polymer powder in a vacuum mixer, forming hardened PMMA [39]. The surgeon uses a drill or an awl to make a small hole in the canal of the femur [36,38]. Reamers are used to gradually widen the canal until a chisel called a rasp can fit to carve the space below the neck, called the metaphysis [38]. The rasp, which is the same size as the actual prosthetic, is placed into the canal in the femur and a trial femoral head is put on to test the components [36,38]. The surgeon puts the ball of the trial head into the socket of the acetabulum and moves it to ensure a proper fit [36,38]. They also test that the two legs are the same length. The surgeon then removes the trial prosthetic and cements or press fits the real one. After ensuring that there are no loose pieces leftover, the surgeon washes, drains and finally closes the wound with sutures [36,38].

After the surgery, the patient must take precautions to avoid motions with a wide range of motion and large loads as these could cause the prosthesis to dislocate [36–38]. Some complications due to THA are infection, blood clots, leg length inequality, dislocation and loosening or wear of the implant [36–38]. Only 1% of patients get an infection [37], 0.3–10% have a dislocation [37], and 3–10% have an instance of deep vein thrombosis [38]. Often when dislocations do occur, they are standalone instances and do not require revision surgeries [37,38].

Revision surgeries are necessary when components loosen, fail or break, or when there is a fracture in the bone around the component [37,38]. Bozic et al reported that the number of THA revisions increased by 23% from 2005 to 2010 because THAs are being

performed on younger patients instead of exclusively elderly patients [40]. Evans et al found that over half of THAs will have a revision within 25 years, and around 25% will have one within 15 to 20 years [41].

5 Critical Review of Current Hip Prostheses

5.1 Components

A total artificial hip joint consists of a femoral stem, femoral head and an acetabular cup (liner and shell) as illustrated in Figure 1 [37, 42–44].

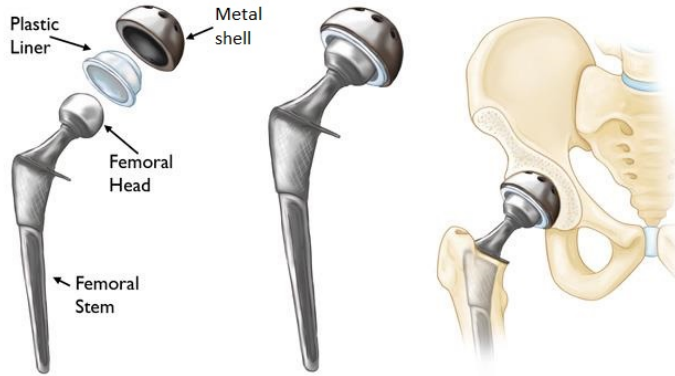


Figure 1: Main components of an artificial hip joint. Modified from [37].

According to the Food and Drug Administration (FDA), there are four main bearing types for total hip implants: metal-on-polyethylene (MoP), ceramic-on-polyethylene (CoP), ceramic-on-ceramic (CoC) and ceramic-on-metal (CoM) [45].

5.2 Geometry

5.2.1 Femoral Stem

Ideally, a cemented femoral stem has a shape that transmits torsional and axial loads to the surrounding cement without producing damaging peak stresses and excessive micromovement [46]. A tapered stem's cross-sectional area decreases in the distal direction and is lodged as a wedge in the cement mantle during axial loading [46]. This reduces

peak stresses in the proximal and distal cement mantle [46]. A successful cementless femoral implant has high stability and promotes bone growth into the porous surface of the implant [47].

5.2.2 Femoral head

The femoral head is a partial ball connected to the neck of the femoral stem [44]. Many studies have shown that the diameter of the femoral head has a significant effect on the quality of a THA [48–50].

Larger femoral head diameters are becoming increasingly popular. As demonstrated in Figure 2, increasing head size given a constant neck thickness (i.e. increasing the head-to-neck ratio) produces a larger impingement-free ROM. This trend no longer holds for head sizes greater than 38 mm, where the hip joint ROM is no longer restricted by implant-implant contact, but rather by tissue-to-tissue impingement [49–51]. It also distributes the stresses as there is a larger contact area [1].

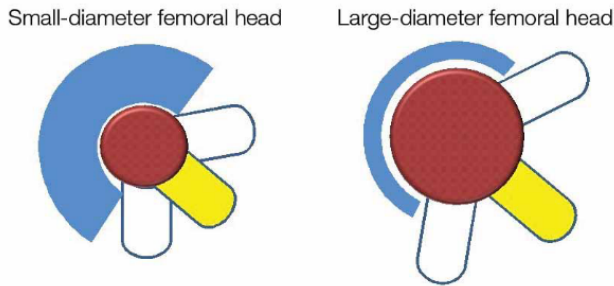


Figure 2: Constricted hip ROM with smaller head size (left) and larger hip ROM with larger head size (right) [50]

Furthermore, larger diameter heads (>36 mm) are less likely to dislocate than smaller heads (<28 mm diameter heads) because larger heads need to travel farther before reaching the edge of the acetabular cup to dislocate. Due to the increased ROM and the reduced risk of implant dislocation provided by a larger head size, hip implant stability is improved with a larger head size [49–51].

One drawback to using 36 mm diameter heads over 28 or 32 mm diameter heads is the increased volumetric wear and frictional moment. This increased wear is experienced

for metal-on-XLPE THAs, but not in ceramic-on-XLPE THAs [51, 52].

5.2.3 Acetabular Shell and Liner

In order for the femoral head to rotate smoothly in the acetabular cup, the liner and shell of the cup need to have a similar curvature to the head. Figure 3 shows three possible polyethylene liner designs [53]. Type A uses a inner chamfer on the liner edge, Type B has a bevelled edge, and Type C has a straight edge.

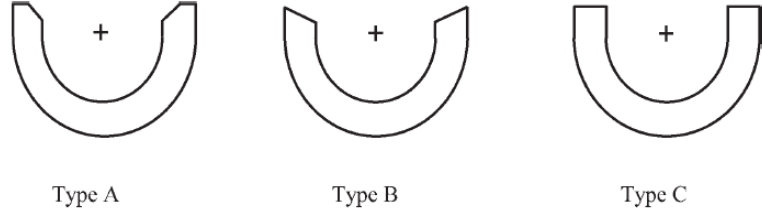


Figure 3: Three types of polyethylene liner designs: Type A (inner chamfer), Type B (bevel), Type C (straight) [53]

Tanino et al used the parameters listed in Table 1 to quantify these three types of geometry. Figure 4 shows the femoral head and acetabular liner along with the relevant measurements for hip stability.

Table 1: Parameters to measure liner geometry

Parameter	Definition
Lip height	Distance from the outer rim of the liner to the head center in the unworn liner contour or the head center in the worn liner contour, denoted as ORu or ORw respectively
Head center inset	Distance from the inner rim of the liner to the head center in the unworn liner contour or the head center in the worn liner contour, denoted as IRu or IRw respectively
Head penetration	3D vector length between the sphere centers in the unworn and worn contours, denoted as HCw

Out of the three geometries, 83% of the liners that have dislocated had an IRu of less than 0.57 mm, and 100% of the liners that have dislocated had an IRu of less than 0.95 mm. Therefore, implementing a polyethylene liner with a depth of more than 0.95 mm

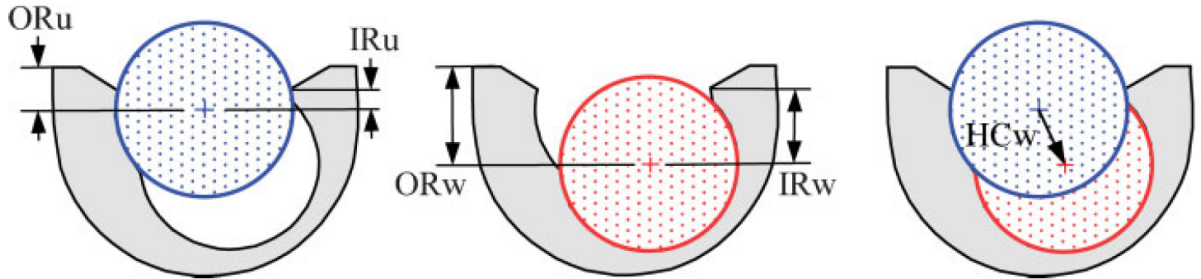


Figure 4: Acetabular liner with relevant measurements for hip stability [53].

may be beneficial in preventing early dislocation. Furthermore, type A (chamfer) liners have the best compromise between a long functional duration and minimal HCw [53].

Hedia et al have conducted finite element analysis to optimize the metal backing for a cemented acetabular cup [54]. The results of their analysis show that cemented acetabular cup designs can be improved by using metal shells that are thick at the dome and thin at the edges [54]. This non-uniform shell thickness minimizes the fatigue notch factor in the cement (shallow curvature around the periphery of the shell) to prevent loosening of the acetabular cup, and increases the fatigue notch factor in the bone at the center of the acetabulum (sharp curvature at the dome) to prevent stress shielding [54]. Hedia et al demonstrated that optimally, the middle of the shell (chosen to be 5.43 mm by the authors) is four times as thick as the edges of the shell (chosen to be 1.24 mm) for a 28 mm femoral head [54]. Literature shows that if a metal-backing is present on a ultra-high molecular weight polyethylene (UHMWPE) cup, it should have a minimum of at least $\frac{1}{4}$ of the femoral head radius. [54, 55]. In addition, other studies show that a shell that is 5 mm thick at the dome and 3.5 mm thick around the periphery preserves more of the natural acetabulum while maintaining the same strength, stiffness and range of motion as a shell that has a uniform thickness of 5 mm [56, 57].

As femoral heads are enlarged, cup and/or liner thickness are reduced in order to maintain the anatomical geometry of the hip [58]. Smaller femoral heads correspond to less volumetric wear in the polyethylene (PE) liner [59]. To account for PE wear while respecting anatomical geometry, the PE liner should be a minimum of 6 mm (but ideally 8 mm) thick [59]. Goebel et al. found that for a 32 mm diameter femoral head, a cup

wall thickness of 5 mm combined with a 8 mm thick UHMWPE liner resulted in low liner deformation, and minimal liner stress under physiological loading at heel strike [58].

5.3 Causes of Hip Implant Failure

A systematic review done by Kenney et al. looked at a total of 9952 THA revisions from 19 studies [60]. Causes for revision surgery were as follows: aseptic loosening (23.19% of failures), instability (22.43%), infection (22.13%) and other modes including mechanical complications, implant failure, fracture, pain, etc. (32.25%) [60]. Friction is generated in the hip implant between the femoral head and the acetabular liner. The moment generated by this friction poses a risk for cup loosening [61–63].

A major factor contributing to the development of instability after THA is the restoration of normal anatomy. As capsular and soft tissue healing takes place in the early post-operative period, instability can occur if the patients exceeds their peri-operative ROM limits. Closed reduction and abduction bracing for six weeks helps prevent this kind of instability. Furthermore, if the implant is designed in a way that does not allow for the new hip motion to replicate natural hip motion, then instability will occur [64].

5.4 Modular vs. Non-modular Hip Implants

A modular femoral stem has a proximal component that attaches to a distal component. Examples of modular fluted titanium stems made by major orthopaedic companies are illustrated in Figure 5 [65]. These include implants from Stryker, Zimmer-Biomet, and Waldemar LINK.

Femoral stem modularity allows for the independent adjustment of size and orientation of the proximal component relative to the distal component. Correct sizing of both components enhances joint stability. In addition, it offers the ability to make small adjustments in vertical and lateral offset to reduce leg-length discrepancy. Studies have shown that modular femoral stems have a survivorship ranging from 94% to 98% at about 10 years after THA. However, there are also disadvantages for femoral stem mod-



Figure 5: Modular fluted titanium stems: A) Restoration Modular (Stryker), B) ZMR (Zimmer-Biomet), C) MP (Waldemar LINK), D) Arcos (Zimmer-Biomet) [65].

ularity. Modular implants pose a risk of failure at the taper junction (e.g. fretting corrosion). Furthermore, modular implants are generally more costly than non-modular implants [65].

Modular dual mobility (MDM) acetabular cups (e.g. Stryker's MDM X3 [66]) are being developed to reduce the risk of THA dislocation. Single mobility acetabular cups allow for relative motion (articulation) between the femoral head and acetabular liner only. In contrast, MDM acetabular cups also allow for articulation between the acetabular liner and acetabular shell. This added articulation increases hip range of motion as demonstrated in Figure 6 [67]. At 15 years follow-up, the survivorship of MDM cups ranged from 81.4% to 96.3% [67, 68].

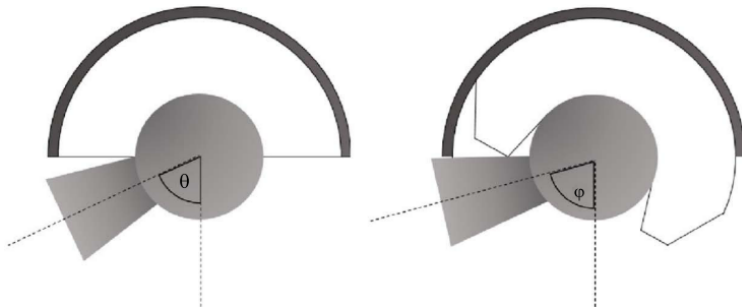


Figure 6: Range of motion of a standard cup (left) and a modular dual mobility cup (right). Modified from [65].

A non-modular hip implant describes a femoral stem piece consisting of the femoral

stem and neck as one solid part. A concern in the use of non-modular stems is the lack of customizability, which reduces the ability to adjust offset, version, and limb length [69]. It has been found that the non-modular stem is an adequate choice as the modular neck stems did not improve hip scores or reduce the possibility of complications or re-operations [69]. Stem modularity is not reported to be worth the risks unless the hip centre cannot be achieved without modularity [69]. It was also found that patients with non-modular stems had lower levels of serum cobalt and chromium in their blood [69]. This is most likely due to the fact that although modular implants fit tightly, there is still the possibility of relative motion causing wear or corrosion. Those with modular implants were also found to have double the prevalence of pseudotumors compared to those with non-modular implants [69].

5.5 Review of an Optimized Hip Prosthesis

Shaik et al designed a hip prostheses by running dynamic finite element analyses (FEAs) for different combinations of femoral head diameters and bearing surface materials. The goal of these analyses was to optimize femoral head size and choice of femoral head and acetabular liner materials. The CAD model of the analysed prosthesis is shown in Figure 7 [70].

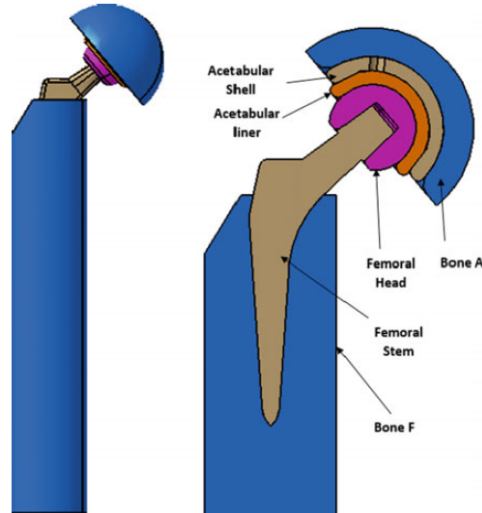


Figure 7: Hip implant model for dynamic finite element analysis [70].

Table 2 lists the dimensions for the three different femoral head and acetabular cup sizes tested [70]. Table 3 shows the femoral stem dimensions used for the analysis [70].

Table 2: Femoral head and acetabular cup dimensions (mm) simulated by Shaik et al. [70]

Head diameter	Liner inner/outer diameter	Shell inner/outer diameter
28	28.02/38	38.02/48
30	30.02/40	40.02/50
32	32.02/42	42.02/52

Table 3: Femoral stem dimensions simulated by Shaik et al. [70]

Length	81.73 mm
Vertical height	24.85 mm
Medial offset	38.58 mm
Neck length	30.03 mm
Taper angle	3.813°
Neck shaft angle	130°

For each of the three head sizes tested, two bearing surface combinations were considered: a ceramic head/ceramic liner (95wt% Al₂O₃, 5wt% 3YSZ), and a metal (Ti6A14V) head/UHMWPE liner. For both bearing surface combinations, the femoral stem was made of Ti6A14V.

The simulations used loading conditions resulting from a 100 kg person jogging at 7 km/h. The resulting hip joint contact force was 4839N and the friction moment was 0.8Nm acting on the femoral head [61, 70].

For the design of Shaik et al, a 30 mm diameter femoral head was chosen since it showed the highest degree of freedom out of the three head sizes tested [70]. The 28 mm head results in dislocation under continuous activity and the 32 mm head experiences more deformation compared to the other sizes [70]. From the simulation, the ceramic head and ceramic liner had the lowest peak Von Mises stress and lowest peak deformation, so the authors chose ceramic bearing surfaces over metal-polyethylene bearing surfaces. [70].

For all head sizes and bearing surfaces simulated, the stress acting on the bone ranges from 7-20 MPa which is substantially less than the yield strength of bone (101-121 MPa). Therefore, these head-size and bearing-surface combinations are capable of adequately

supporting the bone [70].

The wear of the 30-mm diameter head ceramic-ceramic hip was calculated to be 0.062 mm/year. Taking approximately 1 mm of wear to be the threshold for replacement, the hip joint was determined to be safe for 15 years.

The limitation with the 30-mm head ceramic-ceramic hip implant is that ceramic is brittle compared to titanium and polyethylene. Given that elderly people have a higher risk of falls [71], this ceramic hip prosthesis is more prone to fracture if implanted in an elderly patient.

5.6 Fixation Techniques

A hip implant can either be fixated with bone cement (usually PMMA) or can be cementless where it is press fit into the bone. Generally, the cementless approach is used for younger patients, as they will likely outlive the bone cement and they will have more osseointegration to hold the prosthetic to the bone [1]. Osseointegration is the connection or direct attachment between living bone and the surface of a load-carrying implant [72, 73]. In cementless cases, the surface of the prosthetic is usually porous so the bone can attach into the pores as it grows [1]. Often the prosthetic will also have large holes so the bone grows around the prosthetic and surround it [1].

6 Materials Used in Implants

Hip implants can be made from a variety of materials. All materials used in a hip implant must be biocompatible, but each component has different material requirements.

The metal components of hip implants are generally built from titanium alloys, stainless steel or cobalt-chromium alloys [74–76]. Stainless steels are used in hip implants due to their resistance to oxidation, ease of machining, forming and hardening [74]. Stainless steel use in hip implants has declined as stainless steel is not highly biocompatible [74, 77]. Stainless steel implants generally degrade due to pitting and other corrosion mechanisms, releasing metallic particles into the body which can accumulate in tissues [78]. Stainless

steel implants also present an issue due to the increase in nickel allergies and cobalt sensitivities (which are both key components in stainless steel), which can lead to severe allergic reactions and damage to surrounding tissues [78]. The modulus of most medical stainless steels is also much higher than that of bone meaning that it takes much more of the applied forces which can lead to bone degradation and atrophy [77, 79]. This phenomenon is known as stress shielding.

Titanium alloys for implants have become much more popular since the 1970s [80, 81]. Titanium alloys are known for their high corrosion resistance, biocompatibility and excellent mechanical properties [80, 82, 83]. The Young's moduli of titanium alloys are much closer to those of cortical bone than stainless steel, which makes it much more suitable for use in implants [76, 79]. While titanium alloys are suitable for the stem and acetabular component, they are not resistant enough to wear for use in the femoral head [74]. The final common material for hip implants are cobalt-chromium (Co-Cr) alloys. Co-Cr alloys provide good strength, corrosion and wear resistance, making them a common choice for implants [74]. Co-Cr alloys are used as both the material for the femoral stem and the femoral head, since they have sufficient wear resistance [74].

While the materials above provide the appropriate mechanical properties for implants, their usual surface finishes do not support osseointegration [74]. To facilitate osseointegration, porous metals and coatings are used on the surface of the stem [74, 84–86]. Older implants used sintered beads, fiber metal and plasma spray, but these coatings were only bioinert and did not provide high quality osseointegration [74, 85, 87]. A commonly used coating is hydroxyapatite (HA), a bioactive substance which is the inorganic component of bone and facilitates osseointegration [86]. Unfortunately, HA is sometimes absorbed by the body and as a brittle material it can delaminate or release particulates into the body [87, 88]. Porous metals can also be used to encourage osseointegration [84, 85]. Table 4 shows the advantages and disadvantages of different combinations of materials for bearing surfaces. MoP, MoM, CoC, CoP combinations are included.

Table 4: Advantages and Disadvantages of various material combinations for bearing surfaces

Material	Advantages	Disadvantages
MoP	<ul style="list-style-type: none"> • Heavily backed by research [89] • Low cost [89] • Predictable lifespan [89] • Good results in the elderly [74,89] 	Liner wear can lead to debris which can cause osteolysis and loosening [74,89]
MoM	<ul style="list-style-type: none"> • Reduced wear • Longer life than XLPE [74,89] • Lower dislocation rate [74] • Increases ROM [74] 	<ul style="list-style-type: none"> • Co and Cr ions can have negative effects on body [74, 89] • Metallosis which can lead to necrosis [74,89] • Somewhat high rates of osteolysis and failure [74]
CoC	<ul style="list-style-type: none"> • Lower wear rate and friction [74] • Low particle release and release is harmless [89] • Lower osteolysis than MoP and MoM [89] 	<ul style="list-style-type: none"> • High cost [89] • Ceramic can fracture • Noise [74,89]
CoP	<ul style="list-style-type: none"> • Combines advantages of ceramic and PE [74] • Lower wear rate [74] 	<ul style="list-style-type: none"> • Risk of ceramic head fracture [74] • May be some PE wear [74]

7 Gait Analysis

7.1 Normal Gait

A person's manner of walking is referred to as gait. The gait cycle, shown in Figure 8, is known as the series of events that occur between two foot strikes of the same leg, and is split into two components: stance phase (the first 60% of the gait cycle) and swing phase (the final 40%) [90]. Stance phase can be divided into five events; heel contact, foot flat, mid stance, heel off and toe off [91]. Heel contact marks the beginning of stance while toe off marks the end of stance, with mid stance allowing the entire body weight

of the subject to pass directly over the supporting limb (Figure 8). The heel off and toe off events are collectively known as “push-off” due to the limb in stance phase actively pushing against the ground towards the next step [91].

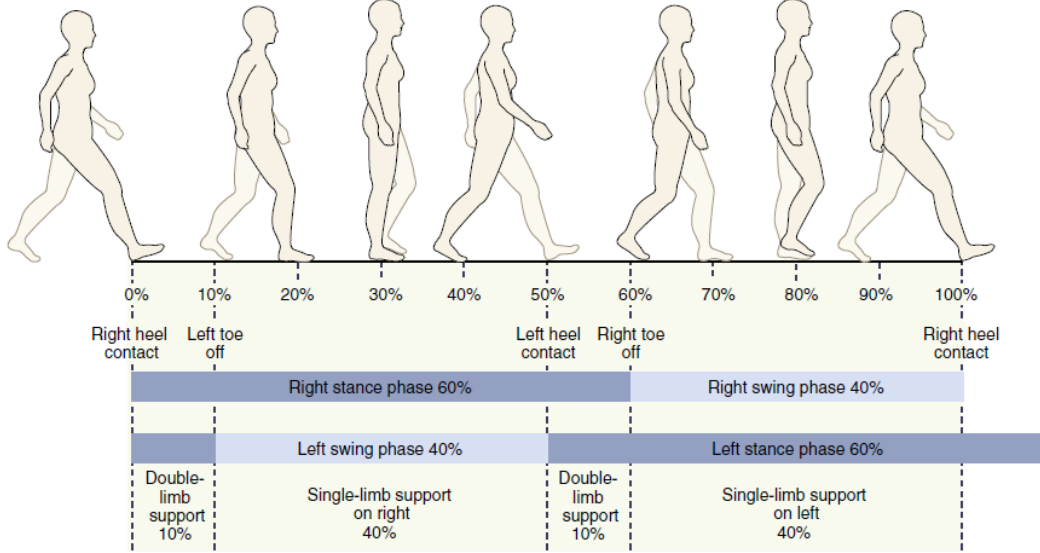


Figure 8: Walking gait cycle [91].

7.2 Ground Reaction Forces

Vertical ground reaction forces (GRF) are the most commonly observed GRF in gait. GRF measurements show a double peak vertically, typically at 30% and 68% stance [90]. Typical GRFs in the first peak equals 1.05 bodyweight (BW), and 1.02BW in the second peak [90]. Patients having received a THA showed to have significant variations in GRFs at the first peak, with the affected limb at 1.02BW and the unaffected limb at 1.06BW [92]. It was also found that the first peak occurred later in stance on the affected limb of those who received a THA (32% as opposed to 29% in control group and the unaffected limb) [92]. The affected limb varied significantly from the control group, and the unaffected limb showed a significant difference compared to the affected limb. Similar variations in force were found in the second peak where that the affected limb had a GRF of 1.00BW and the unaffected limb had a GRF of 1.02BW; however, no significant variation in timing of the second peak was noted [92].

7.3 Hip Kinematics

In the design of a prosthetic hip, it is important that it can provide normal gait for the patient following surgery. The prosthetic must be able to follow the angular displacements of the hip accurately in order to avoid gait abnormalities which often lead to injury or disease of the operated or non-operated limb. It must also be able to withstand the external moments generated at the hip joint throughout gait. This will ensure that the prosthetic does not fail under normal conditions.

The majority of motion in the gait cycle occurs in the sagittal plane, making it the most widely observed plane of motion for gait analysis of the hip. At normal walking speed (1.07m/s), hip angles in the sagittal plane range from -20° to 40° throughout the walking gait cycle [93, 94]. These values vary for each individual, with one standard deviation within control groups going up to as much as 8.9° at certain points in the gait cycle [94]. Hip adduction/abduction angles often range from -12° to 12°, while internal/external rotation angles range from -8° to 0° [94]. Maximum hip flexion angles occur in stair ascent, reaching 67° [94]. The prosthetic design must allow for angular displacement of this value without failure.

A healthy adult has a typical sagittal plane external moment ranging from -0.6Nm/kg at initial contact, to 0.95Nm/kg in mid stance at normal walking speed [1, 94, 95]. Hip adduction/abduction moments range from -0.3Nm/kg to 0.7Nm/kg, while internal/external rotation moments remain quite low, peaking at 0.15Nm/kg [1, 94, 95]. Gait kinematics over the gait cycle can be seen in Figure 9. Stair ascent kinematics differ from walking gait, however the only maximum in magnitude value that results is a maximum external rotation moment of -0.3Nm/kg [96].

THA patients often do not return to normal gait following the procedure, preventing them from participating in recreational activities, therefore lowering their quality of life [97]. Gait parameters were altered in those who received a THA. Patients had a tendency to walk more slowly, have a lower cadence and shorter stride length compared to control groups [98]. The duration of double leg support also increased by 12% and

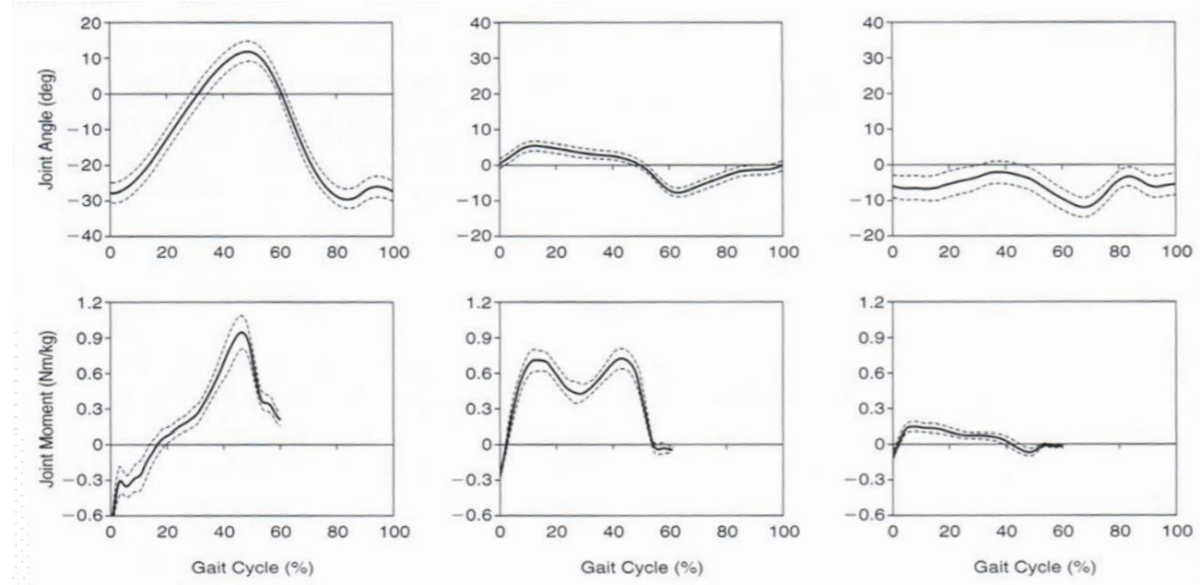
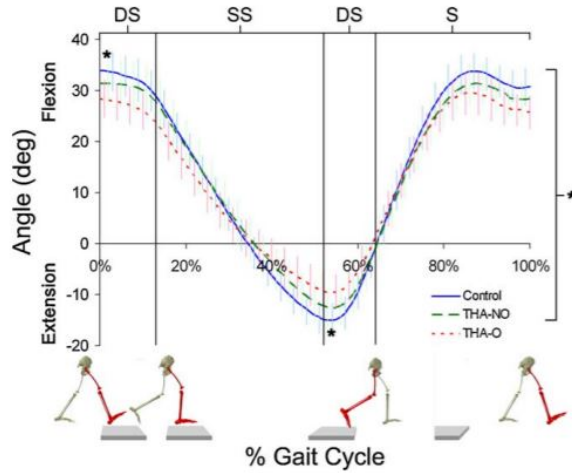


Figure 9: Hip kinematics through the gait cycle. From left to right there is sagittal plane, frontal plane, and transverse plane [1]

single leg support decreased by 4.3% [98]. As seen in Figure 10, patients who received a THA displayed a significantly lower range of motion in the sagittal plane, with a lower peak flexion and peak extension angle, compared to control groups without a THA [97]. THA patients also produced lower peak hip abduction and external rotation moments compared to the control groups [97, 98].



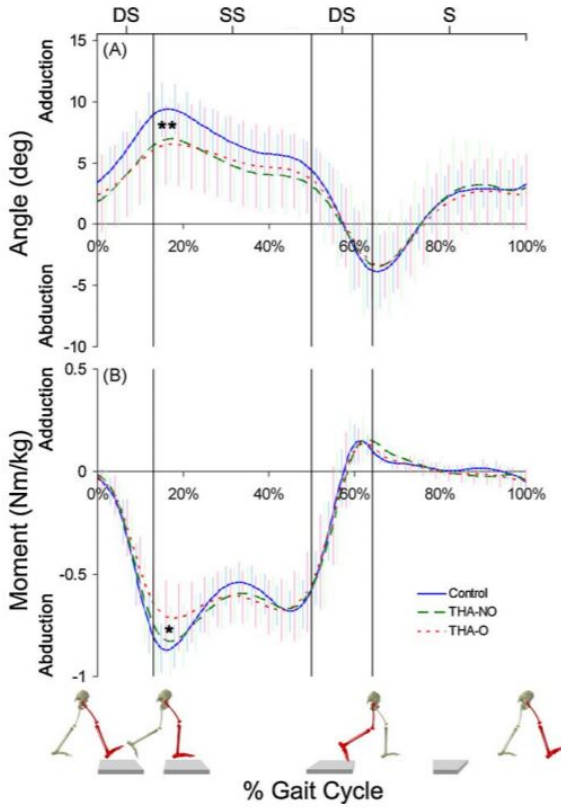


Figure 10: Hip kinematics differences between healthy subjects and THA patients. [97].

7.4 Hip Contact Forces

In order to design a prosthetic hip that will perform as the natural one, the internal contact forces at the hip joint are required. The magnitude and direction of these forces can guide the design of a prosthetic hip that will not displace or break under the hip's maximum loading. During normal walking (4km/h), it was found that the average peak force on the hip was between 211-285% bodyweight (BW) [99]. A previous study by the same authors found peak forces of 307-324% BW, which suggests there is a high level of variability in these forces [99]. A third study by the same author found peak hip contact forces of 290% BW during walking [100]. Stumbling has been shown to cause the highest peak hip contact forces than other daily activities [100]. One study found that the maximum resultant force at the hip rose to 720% BW during stumbling [100].

During stair climbing, one study found the highest implant torque was 83% larger

than during normal walking [99]. This suggests that the stem fixation in the femur should be strong to prevent it from loosening due to high torques [99]. When climbing stairs, the joint contact force was observed to be as much as 251% BW, and 260% BW descending stairs [99]. Figure 11 shows the resultant hip forces for walking and stair climbing for individual patients with THR's and a "typical patient" [101]. In this study, the "typical patient" was calculated as an average of the individuals using a Fourier-based analysis. Femoral anteversion was also observed to be causing high torques on the prosthetic, therefore, inwards torsion of the implant is critical for stem fixation [99].

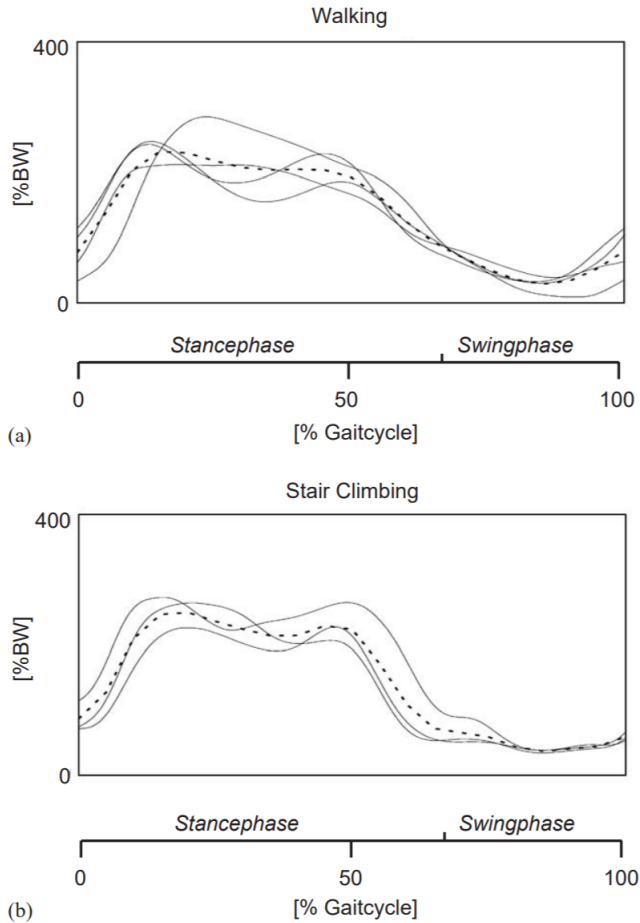


Figure 11: Resultant hip contact forces on an implant for (a) walking and (b) stair climbing. The solid lines represent individual patient data, while the dashed line represents the "typical patient" [101]

The direction of hip contact forces also impacts the longevity of the prosthetic. The

angle of high contact forces in the transverse plane was found to be similar to the normal anteversion angle of approximately 15° [100]. In natural bone, this prevents high bending stresses from generating in the femoral neck [100]. In a prosthetic, loading in the anteversion plane minimizes torsion around the femur's shaft axis, which prevents implant loosening [100]. When planning the surgery, surgeons are encouraged to choose an implant anteversion angle that matches that of the individual before surgery [100].

It has been shown that the calculated hip contact forces are reliant on subject-specific modelling of the hip's geometry [102]. An increase in hip contact forces has been shown with increasing anteversion angle [102]. An increased femoral neck-length was also shown to result in increased hip loading [102]. To improve the calculation of muscle forces and hip loading, medical imaging should be used to determine femoral neck-length, femoral anteversion angle, and hip joint centre for each individual [102].

The dysfunction of a muscle has been shown to increase the joint contact force because a part of the required joint moment is taken over by other muscles with short lever arms, and therefore, higher forces [99]. Similarly, in a person with normal gait, interventions and impairments (such as hip replacement surgery), can increase the loads in bone, muscles and the implant [100]. Load-increasing factors include muscular deficits from surgery, the change in joint geometry from the new implant, and malpositioning of healing fractures [100].

One study generated a musculoskeletal model to predict muscle forces and hip contact forces during walking and stairs [101]. The model was compared with human subjects to be verified. The model determined that it was a reasonable assumption to group the hip muscles into one adductor and one abductor muscle and to remove all muscles providing small forces [101]. The model found the largest resultant hip contact force of 262% BW occurred at the beginning of the gait cycle (early stance phase) [101]. During this same instant, the largest muscle forces were from the abductor (104% BW), the vastus lateralis (95% BW) and the tensor fascia latae (19% BW) [101]. The largest contribution to hip contact forces from two joint muscles came from the semimembranosus (60% BW) [101]. The maximum forces of muscles spanning the hip and knee occurred towards the end of

stance and into swing [101]. These were from the rectus femoris (80% BW), gracilis (27% BW) and sartorius (14% BW) [101]. The maximum gastrocnemius force, which acts on the distal end of the femur, of 31% BW was found at the end of the stance phase [101].

The same study found that with ascending stairs, the maximum resultant hip contact force occurred at the beginning of stance phase as well, but was slightly larger than walking at 278% BW [101]. The anterior-posterior forces acting on the hip were also twice as high as those in normal walking [101]. The abductors force was found to have increased to 114% BW when going up stairs [101]. Specifically, the anterior-posterior component of the abductor force was increased by a factor of 6 [101]. The largest muscle forces calculated during stair climbing were for the vastus lateralis (137% BW) and the vastus medialis (270% BW). The semitendinosus muscle had a peak force of 115% BW during early stance, but other two joint muscles that span the hip and knee had peak forces mainly during late stance and into swing [101].

8 Structural and Functional Analysis of the Hip

8.1 Structural Analysis of the Natural Hip

The primary function of the hip joint is to support the weight of the head, arms and trunk (HAT) while standing and during locomotion [103]. The weight of the HAT passes down through the pelvis to the femoral head and the ground reaction force travels up to the femoral head [103]. These two forces are not collinear; therefore, there is a couple acting on the femur that creates a tensile force and compressive force on the lateral and medial parts of the femur, respectively. The primary weight-bearing surface of the acetabulum is the dome, whereas the primary weight-bearing surface of the femoral head is the superior portion [103].

The key forces acting on the hip joint are the body weight and the force of the abductor muscles. To calculate the reaction force at the femoral head, the free body diagram below (Figure 12) and the law of cosines can be used (Equation 1). In Equation

1, R represents the reaction force, F_M represents the muscle force, and W is the weight of the HAT.

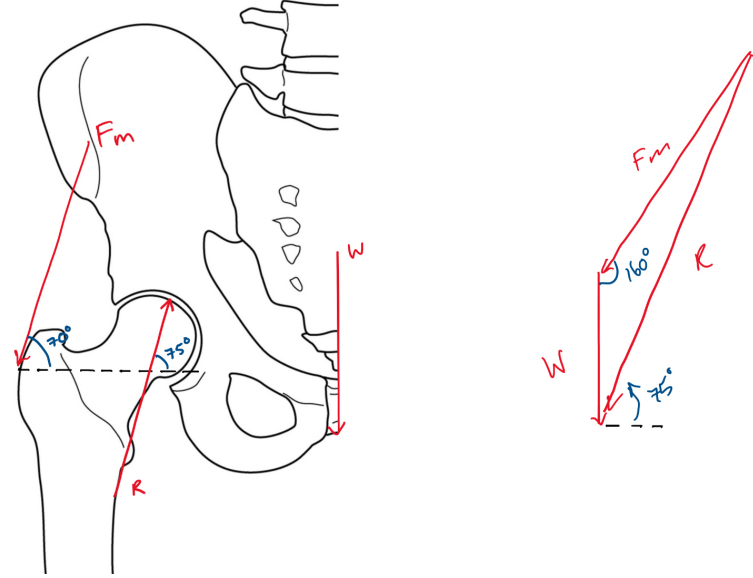


Figure 12: Free body diagram of the hip joint

$$R^2 = F_M^2 + W^2 - 2F_M W \cos 160^\circ \quad (1)$$

In weight-bearing situations, the hip joint is congruent, meaning that the femoral head adopts a similar curvature as the acetabulum [103]. During weight-bearing, the elastic deformation of the acetabulum increases contact with the femoral head [103]. Hip joint congruency reduces the peak contact stress [103]. The hip joint is non-congruent in non-weight bearing situations because the femoral head has more articular surface than the acetabulum [103].

The angle of inclination of the femur (which is 125° for healthy adults) occurs in the frontal plane between a line passing through the femoral head and a line passing through the femoral shaft [103]. Coxa valga is a condition for which this angle is greater than 125° [103]. For this condition, the distance between the femoral head and greater trochanter is decreased and therefore, the length of the moment arm of the hip abductor muscles is also decreased [103]. For coxa vara (an angle of inclination of less than 125°), this

distance is increased, and the femoral head is turned deeper into the acetabulum [103]. Coxa valga therefore increases the demand on the hip abductor muscles to counteract the adduction moment caused by gravity during single-limb support [103]. The opposite is true for coxa vara. Furthermore, for coxa valga, shear and bending stresses across the femoral neck are reduced, resulting in a reduction in the density of the lateral trabecular system. Again, the opposite is true for coxa vara [103].

The angle of torsion of the femur (which is 15° to 20° for healthy adults) occurs in the transverse plane between a line through the femoral head and neck, and a line through the distal femoral condyles [103]. Femoral anteversion occurs when the angle of torsion is greater than 20° and femoral retroversion occurs when this angle is less than 15° [103]. For femoral anteversion, the line of action of the hip abductor muscles may fall posterior to the hip joint, reducing the moment arm for abduction. The opposite is true for femoral retroversion [103].

8.2 Functional Analysis of the Natural Hip

The total artificial hip joint is constructed to mimic the natural hip joint which is a ball-and-socket joint. Just as the femur naturally moves relative to the acetabulum, the femoral stem and head move relative to the acetabular cup. Both the natural and artificial joints are capable of rotating in the sagittal, frontal and transverse planes to produce flexion and extension, abduction and adduction, and internal rotation and external rotation.

In the musculoskeletal system, ROM is the ability of a joint to carry out its complete spectrum of movements [104–107]. Passive range of motion (PROM) is joint movement achieved when an outside force causes the motion (e.g. push/pull of the physiotherapist on a limb), whereas active range of motion (AROM), which is usually less than the PROM, occurs when joint movement comes solely from the contraction and relaxation of opposing muscles [105].

Several studies have been conducted to assess the natural hip PROM and AROM

in healthy adults [108–113]. Approximate averages collected by Svenningsen et al for natural hip PROM, and by Roaas and Andersson, and Roach and Miles for natural hip AROM are shown in Table 5 [109, 111, 113]. In Table 5, the ROM values for hip flexion occur when the knee is flexed. However, when the knee is extended, the range of hip flexion reduces to 90°.

Table 5: Estimated natural hip PROM and AROM (both in degrees) in healthy adults

Motion	Female PROM	Male PROM	Female AROM	Male AROM
Flexion	141	137	121	120
Extension	26	23	19	9
Abduction	42	40	41	39
Adduction	30	29	Not available	30
Internal rot.	52	38	30	32
External rot.	41	43	34	33

Post-operative evaluations of artificial hip ROM have been carried out [114, 115]. Table 6 shows the artificial hip PROM results obtained by Le Duff et al for 35 patients (24 males and 11 females) 96 months after they had undergone bilateral THA [114].

Table 6: Estimated post-operative bilateral artificial hip PROM (in degrees)

Hip motion	PROM
Flexion	121
Extension	Not available
Abduction (in extension)	43
Adduction (in extension)	28
Internal rotation (in extension)	37
External rotation (in extension)	36

These data show that the artificial hip has approximately the same abduction, adduction, internal and external rotation ranges of motion as the natural hip. However, maximum hip flexion is approximately 20° less in the artificial joint than in the natural joint.

Healthy hip ROM for normal gait on level ground is as follows: 30° flexion, 10° hyperextension, 5° of both abduction and adduction, and 5° of both medial and lateral rotation [103].

9 Stability of the Hip Joint

There are several factors affecting the stability of the hip joint. The articular surfaces, ligaments and muscle tone all contribute to the stability of joints. The hip joint is extremely stable due the depth of its ball and socket, meaning that hip dislocations are rare [3]. While the deep socket and strong ligaments of the hip do provide a high degree of stability, they do limit range of motion when compared to the ball and socket joint of the shoulder [3]. Acetabular depth is increased by the acetabular labrum which extends beyond the socket, surrounding the femoral head [3]. The acetabular labrum also contributes to stability by creating a partial vacuum at the joint [116].

In addition, joint stability increases with the number of ligaments [3], but when ligaments are the only factor providing stability, stability is limited [3]. In the hip joint capsule, there are two anterior reinforcing ligaments. The iliofemoral ligament, which resists excessive medial or lateral rotation, is the primary stabilizing component of the anterior hip joint. The pubofemoral ligament ensures a controlled lateral rotation when the hip is extended [103].

Femur structure also influences joint stability. Coxa vara gives the advantage of improved hip stability if the angle of reduction from 125° is not too severe. Femoral anteversion reduces hip stability because the femoral articular surface is more exposed anteriorly [103].

Muscle tone and tendons are generally accepted as the most important factor in the stabilization of most joints [3], but in the case of the hip the depth of the socket and strength of the ligaments provide the majority of the joints stability [3]. The tendons of muscles cross joints and are kept under tension by the constant low level contraction of their muscles, known as muscle tone [3]. The ligaments surrounding the hip joint act to “screw” the femoral head into the socket as the person stands, providing stability [3].

10 Structural and Functional Design Specifications

While the subject in this report is elderly, it is still important to maintain the same range of motion as the biological hip joint as it must allow her to maintain her moderately active lifestyle. This device will be a ball and socket joint like most existing hip replacements, as this design generally allows the closest approximation of the degrees of motion of the hip. The ball should also fit snugly into the cup as to avoid dislocation but still allow for some articulation throughout the full range of motion.

A key aspect of the biological hip joint is the low friction of the synovial joint, allowing for smooth articulation. It is difficult to mimic the properties of the synovial joint as lubricants cannot be included. Instead, low friction materials can be used to provide smooth articulation. There are several possible material combinations including metal on metal, metal on polyethylene, metal or ceramic and ceramic on ceramic. Each combination has its own advantages and disadvantages based on the patient as discussed in Section 6. In the case of an elderly patient polyethylene on metal bearing surfaces have shown good results and are low cost.

Biocompatibility is always an important consideration in the design of artificial joints, as the use of non biocompatible materials can lead to very severe adverse reactions. The particles generated by any wear in the artificial joint should not cause an immune reaction or be greatly corroded by biological fluids.

Despite the age of the patient, the life of the device should still be maximized. If the patient survives beyond the general 15 year life of current hip implants, at the age of 95 they may be too old to properly recover from a new surgery. The life should be maximized to out live the elderly patients.

The selection of materials is also important in terms of osteolysis. Materials with elastic moduli much greater than that of bone can lead to stress shielding, where the bone does not bear much of the load. When the bone becomes unloaded, osteoclasts begin to reabsorb the surrounding bone since it is not needed, which can cause loosening or failure of the implant. In the case of young patients, the surface finish of the implant

should promote cell growth onto the implant. For elderly patients, bone cement is used to fix the implant into the bone as bone growth slows with age. There are additional restrictions for this device which are outlined below:

- Under \$50,000
- For users weighing between 100 and 240 lbs and with a height between 5' and 6'4"
- Maximum device weight of 2kg

11 Static Force Analysis of Biological Joint

11.1 Joint Reaction Forces

A force analysis of the biological hip implant in two static situations was performed using inverse dynamics beginning at the foot. Figure 13 shows the GRF data used for the inverse dynamics analyses. Data obtained from the OpenSim database was normalized and scaled to the weight of the subject studied in this report [117]. It can be seen that the maximum GRF is at 52% gait. This point will be used for the dynamic analysis. Static analyses will be undertaken at the two GRF peaks of loading response and toe off. The anthropometric models used for the static analyses can be found in Appendix A. Sample calculations for loading response can be found in Appendix B.

11.2 Loading Response

Two cases were chosen for analysis at the maximum peaks in the ground reaction forces. The first case chosen was at 18% gait during loading response, the second highest GRF peak. The peak is a repetitive cyclic load on the hip. As mentioned above, GRF forces were obtained from OpenSim. The angles of the limbs were also obtained from OpenSim to be able to match up with the GRF data. Limb dimensions and COMs were determined using anthropometric data from Winter [95]. Winter's data does not provide dimensions for the femoral neck and muscle attachment therefore geometry from various

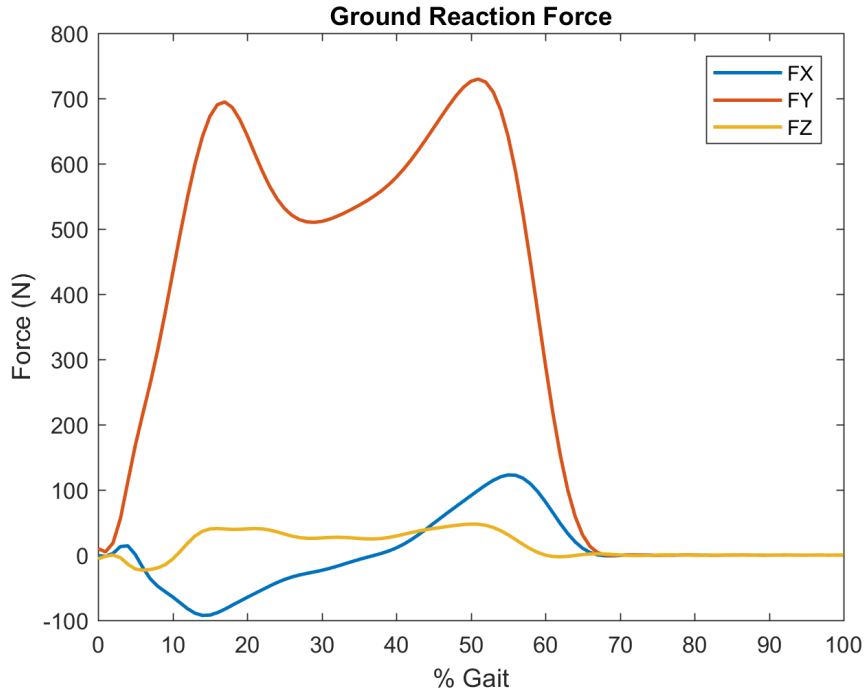


Figure 13: Ground Reaction Forces in the x-, y-, and z-directions

sources was used to determine the location and angle of the muscle force, see E. Table 7 shows the limb angles and GRF at loading response. Table 8 shows the static forces at the hip, knee and ankle joints.

Table 7: Limb angles and GRF at loading response

Variable	Values
Frontal Plane	
Ankle Angle ($^{\circ}$)	-1.7766
Knee Angle ($^{\circ}$)	3.4534
Hip Angle ($^{\circ}$)	4.8758
Sagittal Plane	
Ankle Angle ($^{\circ}$)	0.1417
Knee Angle ($^{\circ}$)	20.1601
Hip Angle ($^{\circ}$)	14.1705
Ground Reaction Forces	
GRFx (N)	-82.8765
GRFy (N)	694.6949
GRFz (N)	40.0229

Table 8: Static forces at the hip, knee and ankle joints at 18% gait

Forces	x (N)	y (N)	z (N)
Ankle			
Force, F_a	82.88	685.41	40.02
Moment, M_a	22.41		2.28
Knee			
Force, F_k	82.88	655.62	40.02
Moment, M_k	143.10		28.60
Hip			
Muscle, F_M		1606.40	
Resultant Contact		1852.10	
Force, F_J	920.32	1663.20	814.84

11.3 Toe Off

The highest GRF peak in the vertical direction occurs during toe-off at 52% into the gait cycle. Table 9 shows the limb angles and GRF at toe off and Table 10 shows the static forces at the hip, knee and ankle joints at toe-off.

Table 9: Limb angles and GRF at toe off

Variable	Values
Frontal Plane	
Ankle Angle ($^{\circ}$)	4.2504
Knee Angle ($^{\circ}$)	3.4338
Hip Angle ($^{\circ}$)	0.9179
Sagittal Plane	
Ankle Angle ($^{\circ}$)	12.1689
Knee Angle ($^{\circ}$)	56.2
Hip Angle ($^{\circ}$)	19.7366
Ground Reaction Forces	
GRFx (N)	99.4268
GRFy (N)	729.7797
GRFz (N)	47.3339

Table 10: Static forces at the hip, knee and ankle joints at 52% gait

Forces	x (N)	y (N)	z (N)
Ankle			
Force, F_a	-99.43	720.43	-47.33
Moment, M_a	-56.34		4.39
Knee			
Force, F_k	-99.43	690.70	-47.33
Moment, M_k	131.22		30.01
Hip			
Muscle, F_M		2055.60	
Resultant Contact		2334.60	
Force, F_J	862.20	2106.10	1007.20

12 Dynamic Force Analysis of Biological Joint

12.1 Foot Analysis

The dynamic force analysis was performed at the largest GRF peak in the y-direction, which corresponds to toe-off at 52% gait. Figure 14 shows the free body diagram of the foot in the frontal and sagittal planes. The GRF in all directions, mass of the foot, and linear and angular accelerations are known for all body segments. The centre of pressure was obtained from OpenSim throughout the gait cycle to match with the GRF forces used for this analysis. The unknown forces and moments exist at the joints in all directions and magnitudes. To solve for these unknown forces, a dynamic analysis is performed. The anthropometric models used for the dynamics analyses can be found in Appendix A.

Equations 2-4 show the summation of forces used to solve for the unknown ankle joint forces in the x-, y-, and z-directions, respectively. In the frontal plane, it was assumed that the centre of pressure, foot COM location, and ankle joint were all in line at the centre of the foot. Table A19 in Appendix C lists the descriptions and values of the variables used for the foot inverse dynamics analysis.

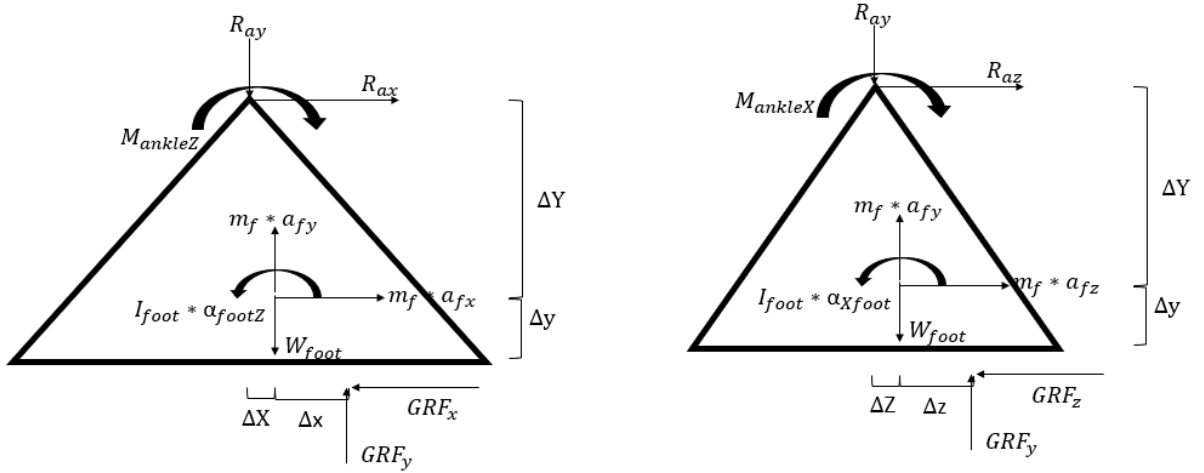


Figure 14: Free body diagram of the foot and ankle in the sagittal (left) and frontal (right) planes

$$\begin{aligned}
 \sum F_x &= m_{foot}a_{fx} \\
 GRF_x + R_{ax} &= m_{foot}a_{fx} \\
 R_{ax} &= m_{foot}a_{fx} - GRF_x
 \end{aligned} \tag{2}$$

$$\begin{aligned}
 \sum F_y &= m_{foot}a_{fy} \\
 GRF_y - R_{ay} - W_{foot} &= m_{foot}a_{fy} \\
 R_{ay} &= GRF_y - W_{foot} - m_{foot}a_{fy}
 \end{aligned} \tag{3}$$

$$\begin{aligned}
 \sum F_z &= m_{foot}a_{fz} \\
 GRF_z + R_{az} &= m_{foot}a_{fz} \\
 R_{az} &= m_{foot}a_{fz} - GRF_z
 \end{aligned} \tag{4}$$

Equations 5 and 6 show the sum of moments about the centre of mass of the foot to

solve for the joint reaction moments about the ankle in the sagittal and frontal planes, respectively.

$$\sum M_{aCOMz} = I_{fz}\alpha_{fz} \quad (5)$$

$$GRF_y\Delta x + GRF_x\Delta y - R_{ax}\Delta Y + R_{ay}\Delta X - M_{az} = I_{fz}\alpha_{fz}$$

$$M_{az} = GRF_y\Delta x + GRF_x\Delta y - R_{ax}\Delta Y + R_{ay}\Delta X - I_{fz}\alpha_{fz}$$

$$\sum M_{aCOMx} = I_{fx}\alpha_{fx} \quad (6)$$

$$-GRF_z\Delta y + R_{az}\Delta Y - M_{ax} = I_{fx}\alpha_{fx}$$

$$M_{ax} = -GRF_z\Delta y + R_{az}\Delta Y - I_{fx}\alpha_{fx}$$

12.2 Shank Analysis

Figure 15 shows the free body diagrams for the shank in the sagittal and frontal planes used to solve for the unknown knee contact forces. At this point in the analysis, the ankle forces and moments in all directions are known, and the only knowns are those at the knee joint. Table A20 in Appendix C lists the descriptions and values used for the shank inverse dynamics analysis at 52% gait.

Equations 7-9 show the summation of forces to solve for the knee joint reaction forces in the x-, y-, and z-directions, respectively.

$$\begin{aligned} \sum F_x &= m_{shank}a_{sx} \\ R_{kx} &= m_{shank}a_{sx} - R_{ax} \end{aligned} \quad (7)$$

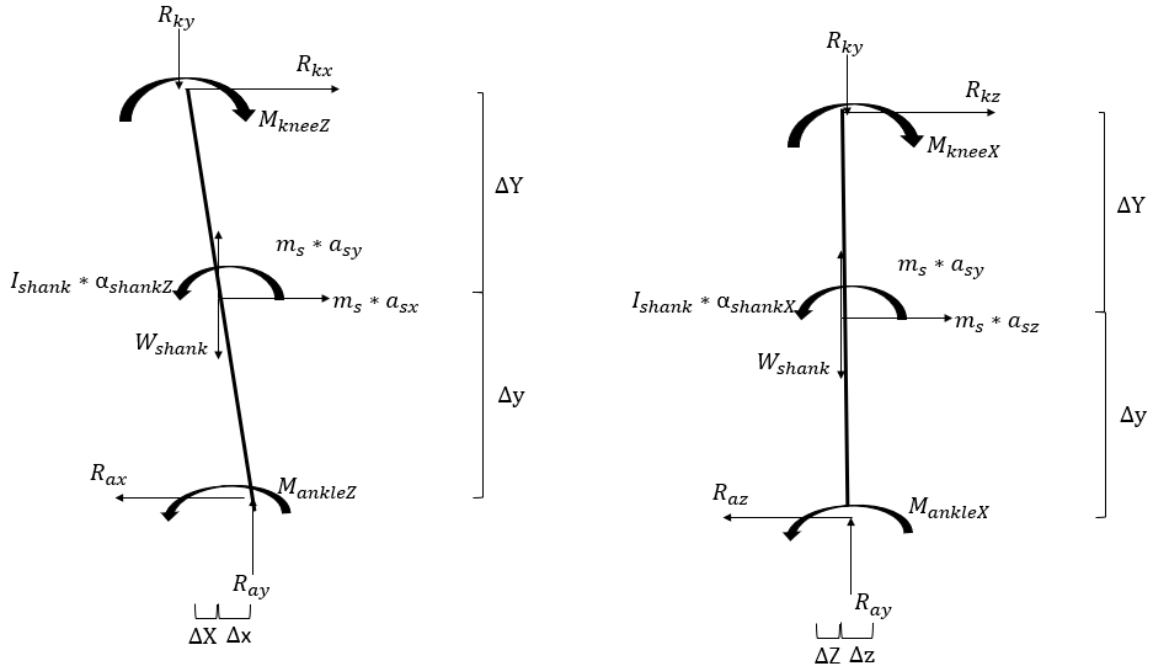


Figure 15: Free body diagram of the shank in the frontal (left) and sagittal (right) planes

$$\sum F_y = m_{shank}a_{sy} \quad (8)$$

$$R_{ky} - = R_{ay} - m_{shank}a_{sy} - W_{shank}$$

$$\sum F_z = m_{shank}a_{sz} \quad (9)$$

$$R_{kz} = m_{shank}a_{sz} + R_{az}$$

Equations 10 and 11 show the summation of moments about the centre of mass of the shank to solve for the joint reaction moments about the knee in the sagittal and frontal planes, respectively.

$$\sum M_{sCOMz} = I_{sz}\alpha_{sz} \quad (10)$$

$$M_{kz} = -R_{ax}\Delta y + R_{ay}\Delta x - R_{kx}\Delta Y + R_{ky}\Delta X + M_{az} - I_{sz}\alpha_{sz}$$

$$\sum M_{sCOMx} = I_{sz}\alpha_{sz} \quad (11)$$

$$M_{kx} = R_{az}\Delta y + R_{kz}\Delta Y - M_{ax} - I_{sx}\alpha_{sx} + R_{ay}\Delta z + R_{ky}\Delta Z$$

12.3 Thigh Analysis

Figure 16 shows the free body diagrams of the thigh in the frontal and sagittal planes. At this point, the knee reaction forces and moments are known. From literature, the joint contact force magnitude and direction is known at the femoral head [118]. Similarly, the frontal plane hip abductor angle was found in literature throughout the gait cycle. Appendix E shows the calculations used to calculate the muscle force angle in the frontal plane throughout the gait cycle. The only unknown is thus the magnitude of the abductor muscle force, F_M , acting at the greater trochanter of the femur. Table A21 in Appendix C lists the descriptions and values of the variables used in the thigh inverse dynamics analysis.

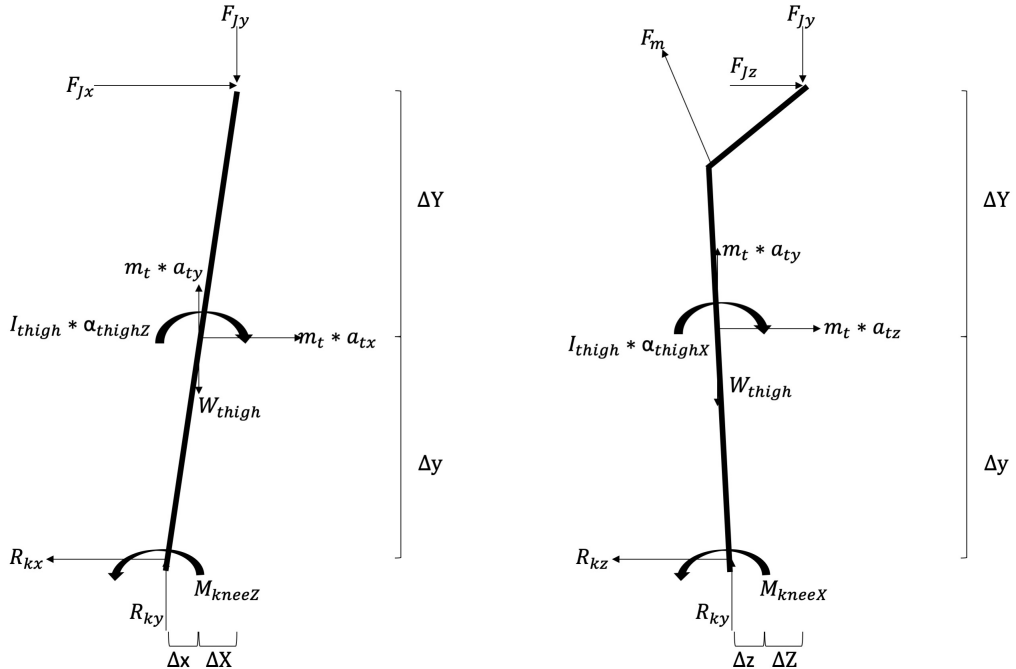


Figure 16: Free body diagrams of the thigh in the sagittal (left) and frontal (right) planes

Equation 12 shows the summation of forces in the y-direction to solve for the resultant

muscle force in the frontal plane.

$$\sum F_y = m_{thigh} a_{ty} \quad (12)$$

$$F_M * \sin(\beta) - F_{Jy} + F_{ky} - m_{thigh} * g = m_{thigh} * a_{ty}$$

$$F_M = \frac{1}{\sin(\beta)} * (F_{Jy} - F_{ky} + m_{thigh} * g + m_{thigh} * a_{ty})$$

12.4 Dynamic Joint Reactions

As mentioned above, the joint contact forces and angles between the femoral head and acetabulum are known. Figure 17 shows the hip contact force angles from the vertical throughout the gait cycle. Figure 18 shows the hip contact force magnitudes throughout the gait cycle. At 52% in the gait cycle, when the GRF is largest, the hip contact force is 1650.2N. The hip contact angle is -32.24° in the frontal plane and is -33.55° in the sagittal plane.

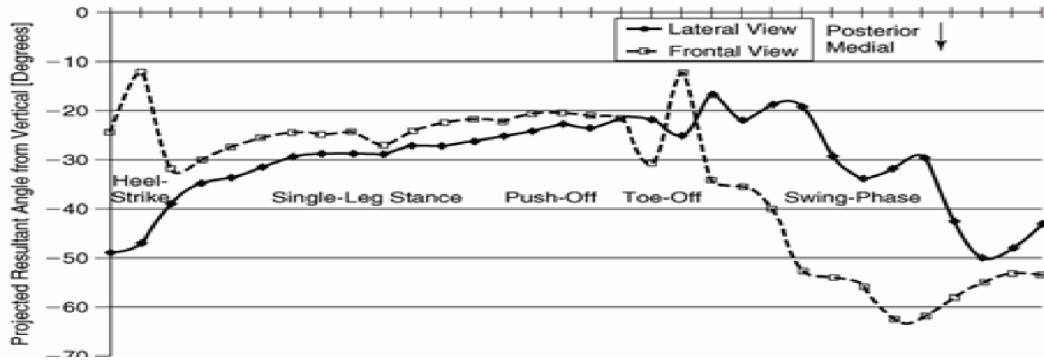


Figure 17: Hip contact angles throughout the gait cycle [118]

For the specific patient chosen for this prosthetic, her femoral neck angle is 126° and femoral neck length is 6.08cm . From trigonometry, this results in a y- and z- distance from the greater trochanter to the femoral head of 3.83cm and 4.72cm , respectively. From literature, the muscle angle of the hip abductor muscles at 52% gait is 69.63° based on the calculation method in Appendix E. Table 11 shows the dynamic joint reaction forces and moments calculated using inverse dynamics. Table 9 shows the joint angles that

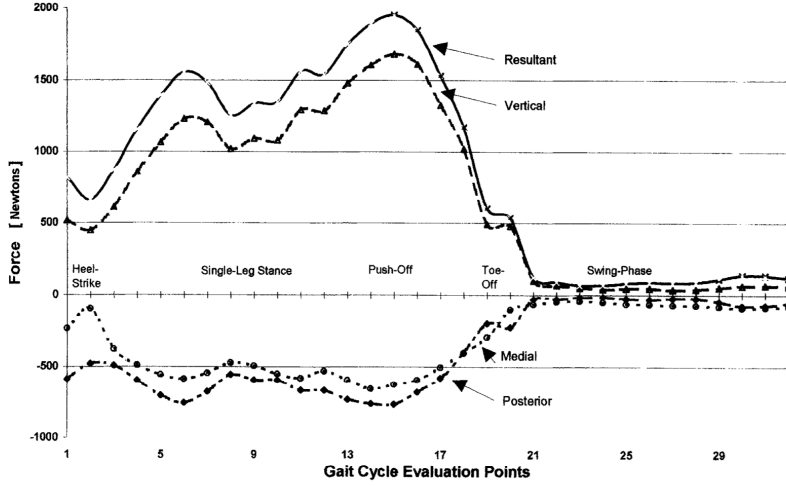


Fig. 1. Acetabular contact force magnitudes in the pelvic reference frame. The acetabular contact force resultant and its relatively large superiorly directed component exhibit the bi-modal pattern characteristic of a force plate pattern (and to which they are related). While the vertical component dominates, the medially directed and posteriorly directed components are substantial.

Figure 18: Hip contact forces throughout the gait cycle [118]

were used for the dynamic analysis at toe-off.

Table 11: Dynamic forces at the hip, knee and ankle joints at 52% gait

Forces	x (N)	y (N)	z (N)
Ankle			
Force, F_a	-96.73	720.5	50.18
Moment, M_a	-2.84		37.3
Knee			
Force, F_k	-84.94	692.54	58.66
Moment, M_k	3.69		15.98
Hip			
Muscle, F_M		815.25	
Resultant Contact		1650.2	
Force, F_J	309.47	1395.8	880.33
Moment, M_h	-291.5		291

13 Chosen Device

The chosen hip implant design for the 70 year old female patient consists of a non-modular stem, a femoral head, an acetabular liner and an acetabular shell as illustrated in Figure 19.



Figure 19: Hip implant design - isometric view on the left, and exploded view on the right (shown in order: acetabular shell, acetabular liner, femoral head and femoral stem)

A non-modular design was chosen for the stem because there were few advantages for this particular patient. The patient is of advanced age, with average anatomical dimensions that would not require specialized stem configurations. Additionally, there is little risk of requiring revision surgery since it is unlikely that the implant will reach its end of life inside the patient.

A cemented fixation method for the stem component was chosen as the user is elderly so new bone growth is minimal. The cement is unlikely to fail before the user's lifetime. Additionally, the use of bone cement is associated with less stress shielding compared to cementless stems, especially in the short term [119]. It has also been found that using cement limits the amount of osteolysis due to particle debris caused by the presence of

the polyethylene liner [59]. The thickness of the cement is 2 mm at all locations because this thickness was found to be within the optimal range to avoid fatigue failure and also limit bone necrosis [120].

The acetabular liner was chosen to be made out of cross-linked PE. This is because the XLPE can provide adequate shock absorption for the patient, will not make noise during movement, and can easily be made in many sizes. There is the risk of wear and debris entering the body, but precautions were taken with the femoral head diameter to reduce the occurrence of wear.

Around the circumference of the liner, there are twelve hemi-cylindrical protrusions that fit into identically shaped slots in the shell, stopping the liner from spinning relative to the shell. Furthermore, the liner has a thin ring that becomes lodged into a cavity on the inner surface of the shell. Once the liner has been press-fit into the shell, this ring prevents the liner from sliding out. An advantage of press-fit liner fixation is the ability to easily replace the liner if it becomes worn out. These design features were inspired from the G7 Acetabular System and the Trilogy IT Acetabular System [121, 122]. To achieve the best compromise between maximum functional duration and minimum wear, the liner design with a chamfer on the inner circular edge (the Type A liner discussed in section 5.2.3) was chosen.

The femoral head is attached to the stem using a triangular shaped protrusion. This shape prevents head rotation on the stem and allows for different sizes of femoral head components to be used. The chosen diameter for the patient is 32mm, which is a mid-range size of implant femoral heads. Since the chosen liner material is XLPE, there is likely going to be wear from the femoral head on the XLPE liner. Compared to a larger diameter head, a smaller diameter head results in less wear, but is also less stable, has less range of motion and puts the user at risk for hip dislocations [49–51]. In this case, a compromise was made to balance the risk of dislocation with the occurrence of wear. The femoral head is made of a Co-Cr-Mo alloy because it has been shown to have better wear properties than titanium alloys and is strong enough to withstand the loads at the hip joint [74].

The acetabular shell was chosen to be thicker at the dome and thinner at the edges to optimize fatigue stress concentration factors, and preserve more of the hip bone while maintaining strength, stiffness and range of motion (as discussed in section 5.2.3).

A recent concern for acetabular cup design was that screw holes in the acetabular shell would provide a passageway for polyethylene liner debris to escape from the cup and cause acetabular osteolysis. Several studies have shown that between solid-backed and cluster-hole cups, there is no significance in the amount of osteolysis and cup migration [123–126]. Therefore, the chosen acetabular shell design contains three screw holes that would give the surgeon the option to use screws for stability if required. If screws are not being used, small threaded inserts are placed in the screw holes [121]. In order for there to be as much bone as possible to screw into, the three screw holes are positioned on the upper side of the acetabular cup in the direction of the ilium of the pelvis.

13.1 Device Components

Figure 20 shows engineering drawings for the acetabular shell. The middle thickness is 5 mm and the edge thickness is 3 mm. Considering the hemi-cylindrical protrusion cuts in the shell, the minimum thickness is 1.25 mm. The middle and minimum thicknesses are close to the optimized thicknesses found by Hedia et al [54].

Figure 21 shows engineering drawings for the acetabular liner. Given that the femoral head diameter is 32 mm and the shell thickness is 5 mm at the dome, a uniform thickness of 8 mm was chosen for the liner in order to account for liner wear, and minimize deformation and stress within the acetabular cup while maintaining anatomical geometry [58, 59]. In addition, a head center inset (denoted IR_u (described in section 5.2.3)) was chosen to be 1 mm to hold the femoral head within the acetabular cup and prevent dislocation.

Figure 22 shows engineering drawings for the femoral head. The head diameter of 32 mm fits in the liner with a diametrical tolerance of 0.02 mm (the same tolerance chosen in the design of Shaik et al [70]). The equilateral triangle cut in the head is 0.01 mm less

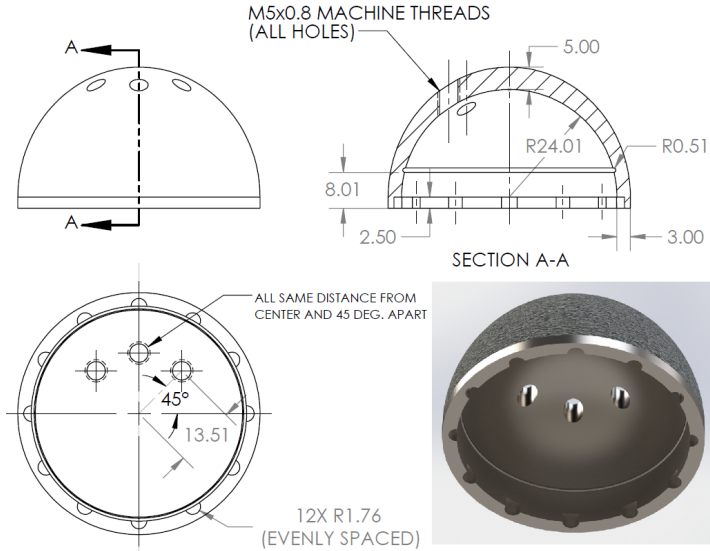


Figure 20: Projected views and render of the acetabular shell (dimensions in mm)

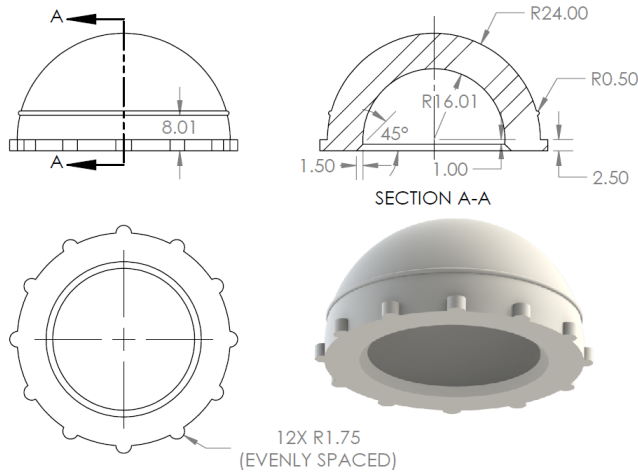


Figure 21: Projected views and render of the acetabular liner (dimensions in mm)

than the triangular protrusion of the stem so that the head can be press-fit on the stem.

Figure 23 shows engineering drawings for the femoral stem. The stem cross-section tapers down from a width of 18 mm to a width of 10 mm. This kind of tapering reduces peak stresses and enhances stem fixation [46, 47]. The stem has a Q-angle of 17° and a neck angle of 126° to respect the anatomical dimensions of the chosen patient. The other stem dimensions were based on standard sizes available in company catalogs [122, 127]. Standard stem sizes are around 150mm, but to attempt to reduce stress shielding, the stem length was shortened to 130mm [127].

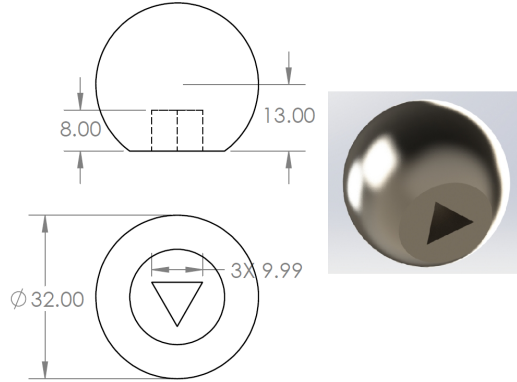


Figure 22: Projected views and render of the femoral head (dimensions in mm)

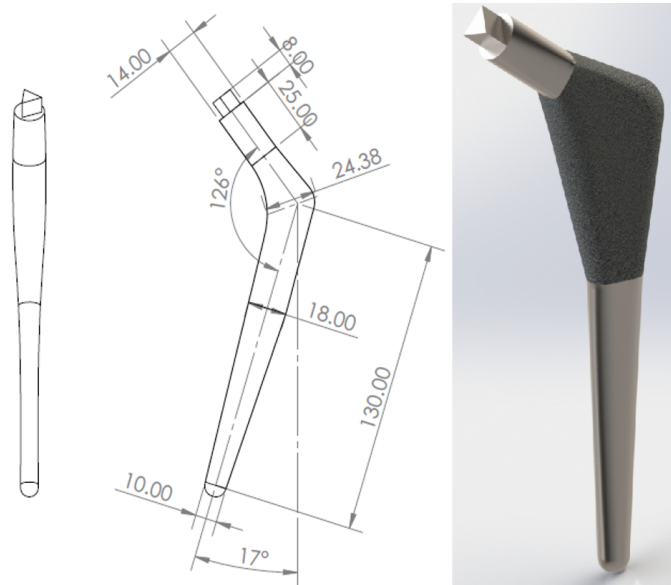


Figure 23: Projected views and render of the femoral stem (dimensions in mm)

13.2 Material Selection

Material selection for medical implants requires the consideration of the four following characteristics: material properties, biocompatibility, corrosion resistance, and ease of medical imaging [1].

Ti-6Al-7Nb is a vanadium free Titanium alloy that has become increasingly popular as an implant material throughout the past two decades [74]. Titanium alloys are a common material selection for medical implants due to their material properties, which have a lower Young's modulus (more similar to that of bone [74]), their excellent corrosion

resistance, and non-magnetic materials, which allows for magnetic resonance imaging (MRI) [74,128,129]. Due to its incorporation of Niobium (Nb), Ti-6Al-7Nb has improved biocompatibility compared to other titanium alloys as Nb is a highly biocompatible material [74]. For these reasons, this Ti-6Al-7Nb has been selected as the material for the stem, neck, and acetabular cup of the implant. The material will have a porous exterior to help secure the cement to the implant.

Recently, Cobalt Chromium (Co-Cr) alloys have become one of the major materials used in hip prostheses [74]. Co-Cr-Mo has been selected for the material of the articulating head of the hip implant. Co-Cr alloys are MRI compatible and biocompatible, with increased corrosion resistance provided by the Chromium (Cr) and the Molybdenum (Mo) [129]. The main advantage of choosing Co-Cr-Mo as the femoral head material is its wear resistance. Due to the higher Young's modulus of this alloy compared to Titanium alloys, the wear resistance is much greater, making it a better selection for the articulating head [74].

The Ti-6Al-7Nb of the neck and the Co-Cr-Mo of the articulating head will be in contact throughout use. Any time there is metal-on-metal contact, galvanic corrosion is a concern. Co-Cr-Mo can be used as a coating for Titanium alloy structures, and has shown no issue of corrosion [130]. Studies have found that Co-Cr alloy/titanium alloy couples are stable [131]. This metal-on-metal interaction should not cause any galvanic corrosion throughout its lifetime.

XLPE has been used in hip prostheses since 1964 [74]. XLPE was developed for increased wear resistance in hip implant bearings while maintaining the mechanical properties of PE [74,132]. XLPE, along with its increased wear resistance, acts as a shock absorber and increases joint stability [1].

Discussed further in Section 13.3, two coatings were selected for this implant. The first coating contains curcumin, which helps inhibit the effects of osteolysis. The second coating is an antibiotic hydrogel which aids in preventing infection post-operation.

13.3 Design Originality

As discussed in section 13.1, the acetabular shell has a non-uniform thickness for optimal fatigue behaviour and bone preservation.

As the user is elderly, bone growth is minimal so cement is used to fix the stem in place. The implant is placed with a superior eccentricity to the center of the cortical bone with the same eccentricity distance that trabecular bone has with the cortical bone in the hip. This superior eccentricity shifts the neutral axis lower, which increases the internal bending moment on a cross section during the majority of gait on the superior location [133]. The superior location is often where the implant loosens so increasing the stress at this point is beneficial, especially near the neck of the prosthesis [133]. In natural bone, the eccentricity increases cortical bone thickness at the inferior side of the bend in the neck, since there would be a higher compressive stress due to the bend in the neck [133]. The implant is placed eccentrically to mimic the natural trabecular bone placement.

One of the disadvantages of using a metal head and PE liner is the wear of the PE, which often releases debris into the body [119, 134]. This causes a reaction from the immune system resulting in osteolysis [119, 134]. This then causes the implant to loosen from the bone as it resorbs. This is most commonly seen in the top of the stem at the edge of the bone as seen in Figure 24 [134].

Periprosthetic osteolysis is the most commonly observed long term complication in THAs [119]. Several studies have shown the positive impact that curcumin (a chemical derived from turmeric) can have on the body, including being anti-inflammatory, anti-cancer, antioxidant and antimicrobial [135]. In this case, the anti-inflammatory properties would inhibit the reaction from the immune system, and reduced osteoclastogenesis [136]. When tested on mice, curcumin had an inhibitory effect on osteolysis caused by debris as it suppressed the RANK protein which is a receptor that activates the production of osteoclasts [136]. Additionally, Virk et al. found a method of making a curcumin coating to be placed on plastics including PEEK [137]. This is done through the technique of

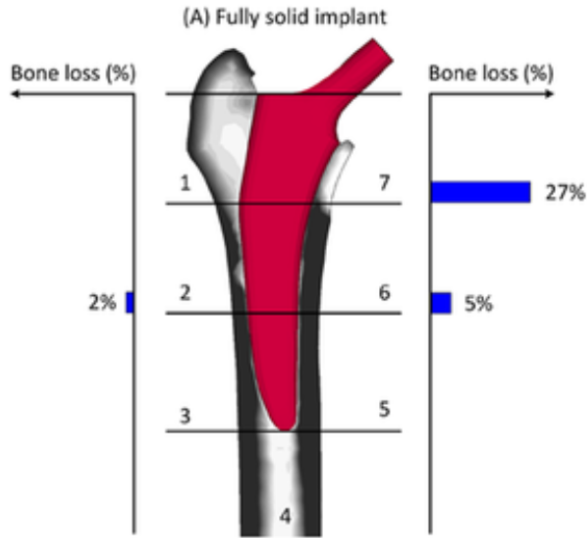


Figure 24: Locations of the femur that are most likely to have osteolysis when the implant is placed [134]

electrophoretic deposition, which deposits coatings on conductive surfaces in suspensions, and has also been shown to be effective for polyethylene. Therefore, the polyethylene liner in the chosen hip implant design is coated in curcumin. The curcumin will be placed on the liner and the upper portion of the stem and neck as this is where loosening is more prevalent [134]. The curcumin would be released slowly overtime, which would not only prevent inflammation as the implant wears, but also provide antibacterial effects [137].

Infection is a major problem contributing to joint prosthesis failure [138]. It was decided to use a fast-resorbable, antibiotic-loaded hydrogel implant coating for the surface of the implant. Coatings of this kind differ from the typical idea of an implant coating. Unlike the aforementioned coating, this gel will be painted on the surface of the prosthesis just prior to implantation into the subject. Substances of this kind undergo full hydrolytic degradation within 72 hours of being in the body [138, 139]. Biocompatible hydrogels of this sort have the ability to provide short term local protection by delivering pharmacological agents while working as a physical barrier to bacterial adhesion [138, 139]. Romano et al. found that Defensive Antibacterial Coating (DAC) was able to provide benefits of reducing the rate of early surgical site infections, without adverse effects such as systemic antibiotic prophylaxis [138].

13.4 Device Range of Motion

The range of motion (ROM) of the designed implant was evaluated in SolidWorks by setting the cup to be fixed and the stem to rotate relative to the cup in the sagittal, frontal and transverse planes. The cup was fixed at a 45° incline [140] in the frontal plane and a 15° anteversion [140] to mimic the natural orientation of the acetabulum with respect to the anatomical planes. Furthermore, the femoral neck is naturally anteverted $15 - 20^\circ$ [103] (a femoral neck anteversion of 17° is assumed for the chosen user of the implant). Therefore, the angle in between the acetabular cup and the femoral neck in the transverse plane was set to 32° ($15^\circ + 17^\circ$).

Figures 25, 26 and 27 illustrate the hip prosthesis' range of motion in the sagittal, frontal and transverse planes, respectively.

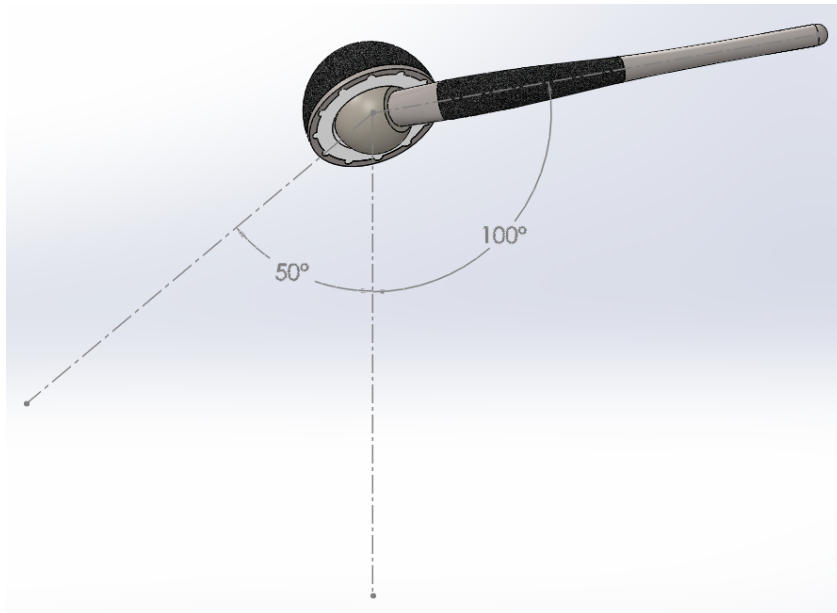


Figure 25: Sagittal plane range of motion of the designed hip implant: 100° flexion and 50° extension

Table 12 compares the prosthesis' ROM to the natural and post-operative bi-lateral hip replacement ROM values mentioned in Section 8.2.

All prosthetic ROM values exceed female PROM and post-operative ROM values for all motions, except for flexion. Therefore, natural motion impingement will be maintained

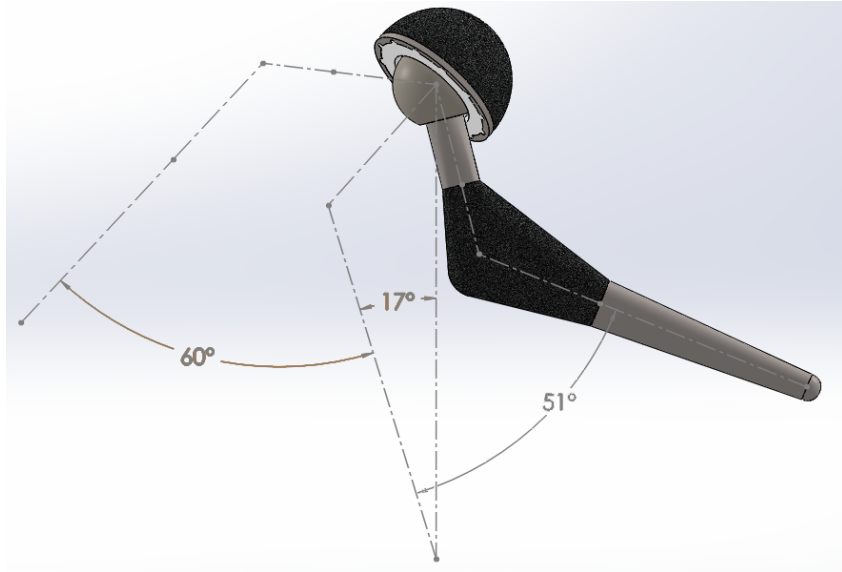


Figure 26: Frontal plane range of motion of the designed hip implant: 51° adduction and 60° abduction

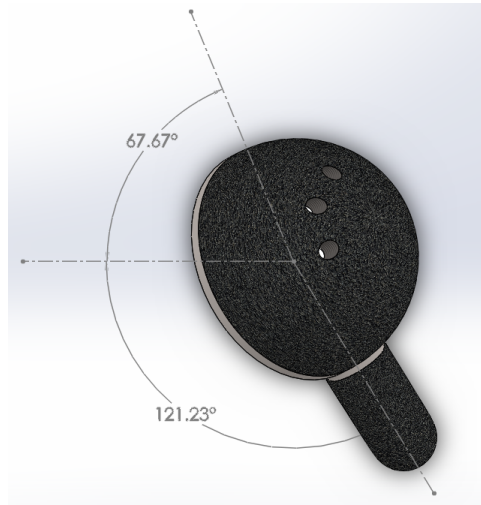


Figure 27: Transverse plane range of motion of the designed hip implant: 121.23° internal rotation and 67.67° external rotation

for all hip motions except for flexion. The values in Table 12 are for healthy middle aged individuals. However, the range of hip flexion decreases with age [141]. For elderly people aged 55-86, the range of hip flexion is $109 \pm 19^\circ$ [141], meaning that for the chosen elderly woman as the user, the hip implant flexion of 100° is reasonable.

Table 12: Prosthesis ROM compared to ROM values relevant to the elderly female user (units in degrees)

Hip motion	Hip implant ROM	Female PROM	Post-op ROM
Flexion	100	141	121
Extension	50	26	23
Abduction	51	42	40
Adduction	60	30	29
Internal rotation	121.23	52	38
External rotation	67.67	41	43

14 Stress Analysis

14.1 Analysis of the biological joint

All stress analyses were calculated at the frame in gait where the forces are maximum, which is at 52%, calculated through static inverse dynamics. The cancellous and cortical bone in the femur are not concentric to reduce the tensile risk of fracture during gait, as the load will not be shared evenly, and the majority of it will be taken by the stronger cortical bone [133]. Figure 28 shows the eccentricity of the cortical and cancellous bone [133]. The Composite Beam Theory will be used to analyze the stresses at point s and i, in the thinnest part of the femoral neck, found in Appendix D.

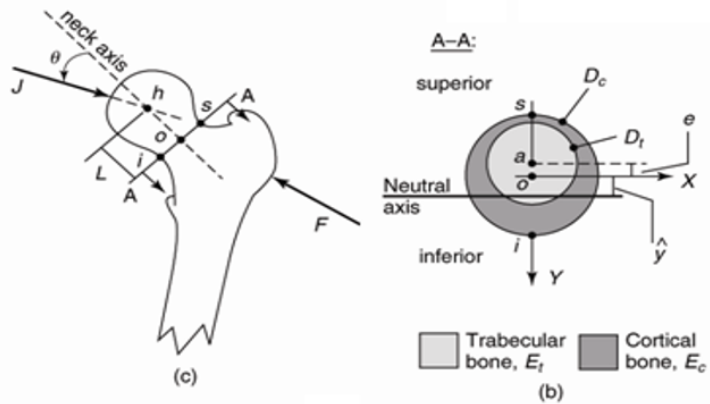


Figure 28: Bone forces and eccentricity. J represents the bone contact forces, s and i are the analyzed critical points, e is the eccentricity distance, and L is the perpendicular distance from the center of the head to the cross section of interest. [133]

Table 13 shows the results for the stresses in the cortical bone at various cross sections seen in Figure 29. These calculations are merely estimates, as it was not possible to obtain an accurate diameter for the trabecular and cortical bone at these sections.

Table 13: Stress Analysis for the natural bone implant at 3 cross sections

	B-B	C-C	D-D
P (N)	-1517	-254.2	-254.2
V (N)	1773.6	-205.2	-205.2
M(Nm)	28.6	-17.6	-17.6
Axial (MPa)	-0.5	-0.26	-0.25
Bending Moment Stress (MPa)	6.2	-17.9	-135.9
Total σ	57	-16.5	-136.1
Safety Factor	35.8	22.7	1.5

14.2 Analysis of the Bone and Implant

A similar method is used to analyze the stresses in the bone and implant together. In this case, there are three components to the composite: the concrete, the implant and the cortical bone. Stress calculations can be found in Appendix D. Four different cross sections were analyzed, as seen in Figure 29.

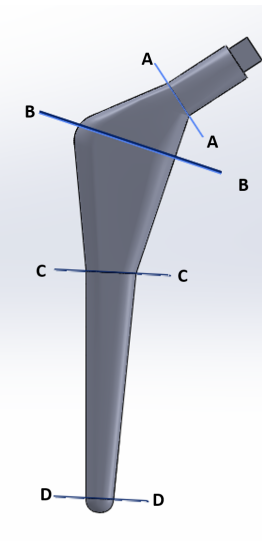


Figure 29: Analyzed sections of the prosthetic for the stress analysis

For each of the cross sections, the general geometrical data can be found in Table

14. The distances Z_J and Y_J are the distance from the location of the contact force to the analysed cross sections, and the distances Z_M and Y_M are the distances from the application of the muscle force to the cross section. In all cases where there is both bone, cement, and implant, the eccentricity of the implant is located 0.7mm from the center of the cortical bone, to mimic the trabecular eccentricity in the natural bone.

Table 14: General geometrical variables used in the stress analysis 29

	A-A	B-B	C-C	D-D
Diameter (max) of implant (m)	0.015	0.023	0.015	0.01
Diameter of cortical bone (m)	-	0.05	0.028	0.028
Moment of Inertia implant ($m^4 * 10^{-9}$)	2.49	47.01	3.54	0.44
Moment of Inertia cement ($m^4 * 10^{-9}$)	-	78.8	5.11	1.31
Moment of Inertia bone ($m^4 * 10^{-9}$)		113.7	21.5	28.8
Distance Z_J (m)	0.041	0.036	0.021	0.0021
Distance Y_J (m)	.014	0.047	0.094	0.172
Distance Z_M (m)	-	-	0.033	0.057
Distance Z_M (m)	-	-	0.046	0.124

In Section A-A, located at the edge of the neck, there is no cement or bone, and therefore this section is not a composite beam. Both sections A-A and B-B do not have the muscle force included in the calculation as the cross section is cut before or at the location of the muscle insertion. Contributions from the x-direction were neglected in all sections as the forces and distances were minimal.

The cross section at section C-C for the metal implant and it's dimensions are seen in Figure 30a. The entire cross section at C-C including the bone, cement and implant is found in Figure 30b. The sample calculations are for the diagram depicted in Figure 31.

The results of the stress analysis are summarized in Tables 15 to 17. The safety factors for each cross section are also calculated. The ultimate tensile stress for femoral cortical bone, PMMA bone cement, and Titanium are 205, 34, and 995 MPa, respectively [142–144].

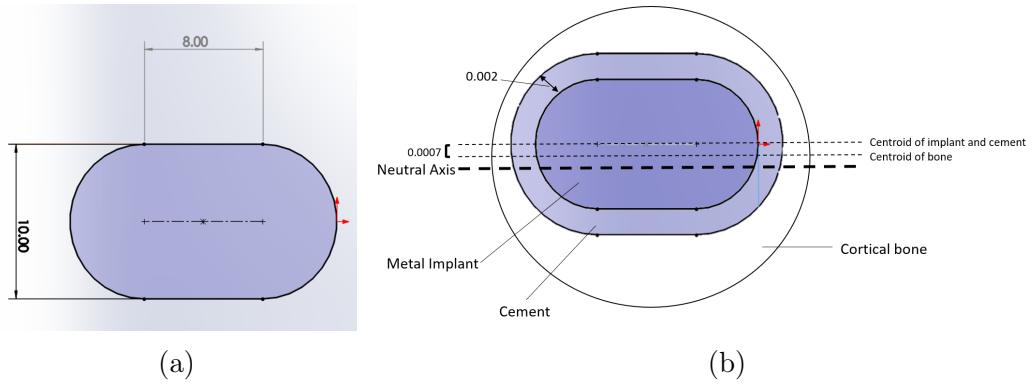


Figure 30: a) The implant cross section dimensions b) The entire cross section at section C-C

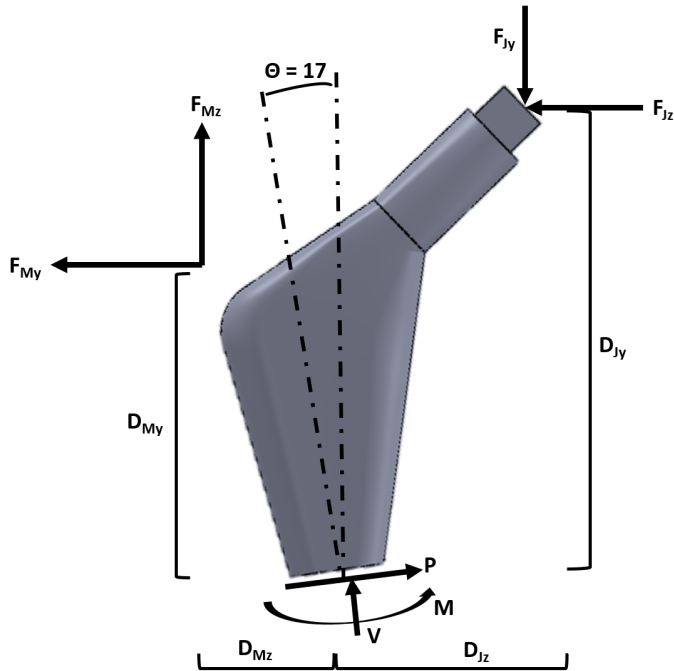


Figure 31: Free body diagram for stress analysis at section C-C

Table 15: Stresses in the implant for all cross sections from Figure 29

	A-A	B-B	C-C	D-D
P (N)	-1637.97	-1516	-254.2	-254.2
V (N)	1663.35	1773	-205.2	-205.2
M(Nm)	71.52	28.6	-25.3	-151.1
Axial (MPa)	-9.28	-2.68	-1.1	-1.68
Bending Moment Stress (MPa)	-215	5.6	-29.8	-156.3
Maximum σ	-225.1	0.89	51.9	-157.9
Safety Factor (MPa)	4.4	338	32	7.6

Table 16: Stresses in the bone for all cross sections from Figure 29

	A-A	B-B	C-C	D-D
P (N)	-1637.97	-1516	-254.2	-254.2
V (N)	1663.35	1773	-205.2	-205.2
M(Nm)	71.52	28.6	-25.3	-151.1
Axial (MPa)	-	-0.04	-0.20	-0.28
Bending Moment Stress (MPa)	-	-0.06	-8.90	-70.19
Maximum σ (MPa)	-	-1.60	-9.1	-70.48
Safety Factors	-	128.23	22	2.9

Table 17: Stresses in the cement for all cross sections found in Figure 29

	A-A	B-B	C-C	D-D
P (N)	1286.8	1211.6	777.5	777.5
V (N)	1022.15	1120.4	-377.43	-377.43
M(Nm)	1286.79	9.79	-44.37	-141.4
Axial (MPa)	-	-0.04	-0.07	-0.12
Bending Moment Stress (MPa)	-	0.06	-1.29	-6.27
Maximum σ (MPa)	-	0.23	-1.1	-6.39
Safety Factors	-	1457	31	5.3

14.3 Stress Shielding

Stress shielding is inevitable in the bone after the implant is added, as the implant is much stronger than the original trabecular bone it is replacing. The goal of this design is to minimize the stress shielding as much as possible. The geometry of the implant was iterated several times to reduce the amount of stress shielding. After the calculations, it is observed that the maximum stress shielding occurs at the second cross section analyzed (B-B). Although there is some stress shielding, it would be increased with a different material, a wider stem, or a poorer fixation to the bone. The ratio of natural bone stress to stress on the cortical bone with the presence of an implant is 3.5 times (72%) at cross section B-B, 1.8 times (45%) at cross section C-C and 1.4 times (27%) at cross section D-D. This shows that as the implant tapers, the natural bone is taking the same load as it would without the presence of the implant, which is similar to other studies found in literature [145].

14.4 Contact Stresses

A Hertz theory analysis is done on the contact location between the acetabular liner and the implant femoral ball. The maximum contact pressure between them is 146MPa. In the natural bone, the maximum contact stress is 502MPa.

To calculate the safety factors, the Langer criteria is used since there is a cyclic load on the implant. The Modified Goodman Criteria was not used because the XLPE does not have an endurance limit. To determine the safety factors, the maximum and minimum stresses need to be determined. The maximum stress (σ_{max}) is the stress calculated for the static toe off case. The minimum stress (σ_{min}) is for a case where only the muscle force was acting on the implant. The minimum stress is found to be 145.33MPa. The safety factors for the XLPE and Co-Cr are 4.2 and 6.5 respectively in the implant case. The calculations can be found in Appendix D

14.5 Wear Analysis of the Acetabular Liner

Although there are low frictional forces between the acetabular liner and the femoral head of the prosthetic, wear of the liner is still prominent. Equation 13 calculates the volumetric loss by wear, V , where K is the wear coefficient, P is the normal force acting on the liner, L is the sliding distance, and H is the Brinell hardness.

For XLPE with a density of 1080kg/m^2 , the wear coefficient is 1.3×10^{-7} [146]. For the worst case scenario, the largest sliding distance would be the distance travelled across the diameter of the liner. Half of the circumference of the inner diameter of the liner will be equal to that of the femoral head, given by $L = 2 * \pi d$. The Brinell hardness of XLPE is 360HB [147]. The SI units of Brinell hardness are kilogram force per millimeter squared. To convert this to Newtons per millimeter squared, the hardness can be multiplied by the acceleration due to gravity

$$V = K \frac{PL}{3H} \quad (13)$$
$$V = 1.3 \times 10^{-7} * \frac{1650.2 * 2 * \pi * 32}{3 * 360 * 9.81}$$
$$V = 4.07 \times 10^{-6} \text{mm}^3/\text{step}$$

For a lifetime of 10 million steps on the implant leg (approximately 10 years), this would result in 40.7mm^3 of wear from the XLPE, which is equivalent to a $3.4 \times 3.4 \times 3.4\text{mm}$ cube.

14.6 Fatigue Analysis of Femoral Stem

As the individual walks, there are alternating cyclic stresses on the femoral stem. Even as the patient is laying down, the muscle forces acting at the greater trochanter and around the hip act to push the implant into the acetabulum. The femoral stem is made of Ti-6Al-7Nb, which has an endurance limit of approximately 600MPa when made by casting processes [148]. The yield stress of Ti-6Al-7Nb is 905MPa and the UTS is

1005MPa.

For the fatigue analysis, the minimum force applied to the femoral head was assumed to be equal to the muscle force, calculated as $F_{min} = 815.25N$ in compression. This would be the case for if the individual was laying down. The maximum force was taken as the joint reaction force calculated previously, as $F_{max} = 1650.2N$ in compression. The mean and alternating stresses were calculated using these values.

$$F_m = \frac{F_{min} + F_{max}}{2}$$

$$F_m = -1232.7N$$

$$F_a = F_{max} - F_m$$

$$F_a = -417.5N$$

Table 18 shows the cross-sectional areas and alternating and mean stresses calculated for each section of the femoral stem. The equations in Appendix D were used to calculate the stresses using both the minimum and maximum forces. Figure 32 shows the modified Goodman line along with the mean and alternating stresses of each cross section. Equation 14 shows how the modified Goodman line is calculated, where σ_a is the alternating stress, σ_m is the mean stress, σ_e is the endurance limit of Ti-6Al-7Nb, and σ_u is the UTS. The modified Goodman line is composed of the Goodman line, connecting the endurance stress on the y-axis with the UTS on the x-axis, and a line connecting the yield stress on the x- and y-axes. It is clear that all cross-sections have combinations of mean and alternating stresses that are well within the safe zone of the modified Goodman chart.

$$\frac{\sigma_a}{\sigma_e} + \frac{\sigma_m}{\sigma_u} = 1 \quad (14)$$

Table 18: Cross-sectional areas and stresses in femoral stem

Cross-Section	Area (mm^2)	Alternating Stress (MPa)	Mean Stress (MPa)
A-A	193.82	35.7	105.6
B-B	498.25	0.22	0.66
C-C	158.58	14.7	34.01
D-D	68.21	41.5	109.9

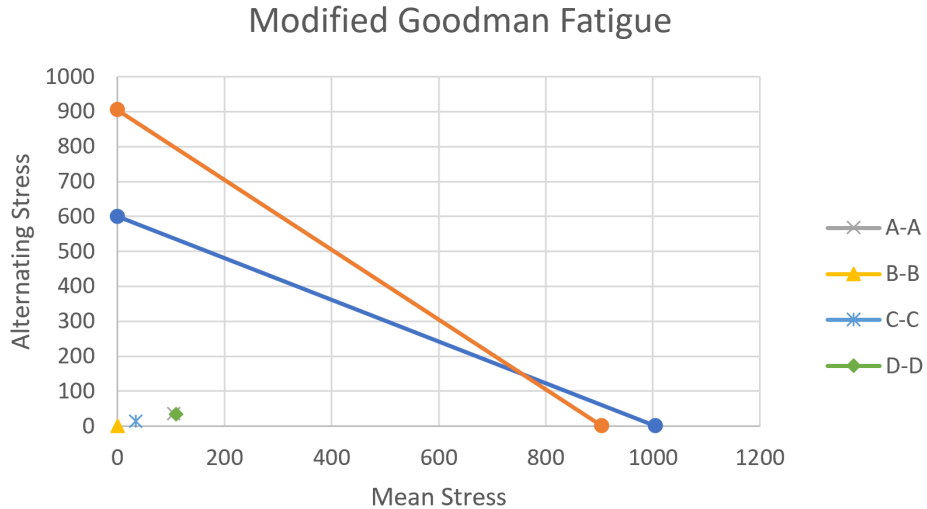


Figure 32: Modified Goodman fatigue diagram for four cross-sections of the femoral stem

15 Testing and Evaluation Methods

To test prostheses, finite element analysis is often used. This would involve using the chosen materials and their properties and applying the calculated forces to analyze stresses in the entire 3D model. Additionally, the ASTM F2068 published standards for testing metallic implants before using them in the body [149]. The ISO relating to hip implants is ISO 7206 [150]. This includes the stem fatigue test, the femoral neck fatigue test and the hip wear test [151]. The stem fatigue test consists of applying a sinusoidal force of 2300N at 9° medial and 10° anterior from the stem axis [151]. The neck fatigue test is the same procedure but with 5340N, based on natural joint contact force calculations [151]. The test is performed for $5 * 10^6$ cycles. loading rate has only a minor influence on the fatigue properties [151]. For this report, the only analysis

performed was with the Composite Beam Theory.

16 Conclusion

The design for this implant aims to reduce stress shielding, reduce chance of osteolysis, maintain range of motion and natural kinematics, mimic the natural bone and not prematurely fracture. The prosthesis is cemented into place as the user is elderly and bone growth is minimal. The user was chosen to be a 70 year old female as this was the most common age and gender requiring THAs. A cross linked polyethylene liner that snaps into the acetabular metal shell was chosen so that it can be easily replaced if it wears out. A mid range head size was chosen (32mm) to maintain range of motion, prevent dislocations, distribute stresses, and not overly increase wear. To prevent osteolysis, a curcumin coating is placed on the upper part of the stem and neck to inhibit the proteins that create osteoclasts from the presence of debris. An additional antibiotic hydrogel coating is placed on the implant to prevent infection. The implant is placed eccentrically in the bone to mimic trabecular bone. A metal on polyethylene bearing surface limits fractures and increases strength. The material for the head is Co-Cr since it has been shown to wear less compared to Titanium. The acetabular shell has a nonuniform radius to optimize fatigue stress while preserving as much of the natural acetabulum as possible. The implant was found to have a life that would exceed that of the user.

References

- [1] M. Doumit, “Design of Artificial Joint Prostheses and Implants - Note 9: Total Hip Replacement,” pp. 1–36, 2019.
- [2] “Anatomy of Hip.” [Online]. Available: <https://www.arthritis.org/about-arthritis/where-it-hurts/hip-pain/hip-anatomy.php>
- [3] E. Marieb and K. Hoehn, *Human anatomy and Physiology 9th Edition*, 2013.
- [4] R. C. Lawrence, C. G. Helmick, F. C. Arnett, R. A. Deyo, D. T. Felson, E. H. Giannini, S. P. Heyse, R. Hirsch, M. C. Hochberg, G. G. Hunder, M. H. Liang, S. R. Pillemer, V. D. Steen, and F. Wolfe, “Estimates of the prevalence of arthritis and selected musculoskeletal disorders in the United States.” *Arthritis and rheumatism*, vol. 41, no. 5, pp. 778–99, 5 1998. [Online]. Available: <http://www.ncbi.nlm.nih.gov/pubmed/9588729>
- [5] R. C. Lawrence, D. T. Felson, C. G. Helmick, L. M. Arnold, H. Choi, R. A. Deyo, S. Gabriel, R. Hirsch, M. C. Hochberg, G. G. Hunder, J. M. Jordan, J. N. Katz, H. M. Kremers, and F. Wolfe, “Estimates of the prevalence of arthritis and other rheumatic conditions in the United States. Part II,” *Arthritis and Rheumatism*, vol. 58, no. 1, pp. 26–35, 1 2008.
- [6] “Hip Replacement Surgery | Johns Hopkins Medicine.” [Online]. Available: <https://www.hopkinsmedicine.org/health/treatment-tests-and-therapies/hip-replacement-surgery>
- [7] F. Berenbaum, “Osteoarthritis as an inflammatory disease (osteoarthritis is not osteoarthrosis!).” *Osteoarthritis and cartilage*, vol. 21, no. 1, pp. 16–21, 1 2013. [Online]. Available: <http://www.ncbi.nlm.nih.gov/pubmed/23194896>
- [8] J. Samuels, S. Krasnokutsky, and S. Abramson, “Osteoarthritis: A tale of three tissues,” *Bulletin of the NYU Hospital for Joint Diseases.*, vol. 66, no. 3, pp. 244–250, 2008.
- [9] A. Hafez, A. Alenazi, S. Kachanathu, A. Alroumi, and E. Mohamed, “Knee Osteoarthritis: A Review of Literature,” *Physical Medicine and Rehabilitation International*, vol. 1, no. 5, p. 8, 2014.
- [10] M. Bonnin and P. Chambat, *Osteoarthritis of the Knee - Surgical Treatment*. Springer, 2008.
- [11] V. B. Kraus, F. J. Blanco, M. Englund, M. A. Karsdal, and L. S. Lohmander, “Call for standardized definitions of osteoarthritis and risk stratification for clinical trials and clinical use,” pp. 1233–1241, 8 2015.

- [12] P. E. Di, C. Dominik, R. H. Jonathan, and S. Steven, *CONNECTIVE TISSUE DISORDERS Pathogenesis of Osteoarthritis*. Elsevier Inc. [Online]. Available: <http://dx.doi.org/10.1016/B978-0-323-31696-5.00098-X>
- [13] J. Loughlin, “The genetic epidemiology of human primary osteoarthritis: current status.” *Expert reviews in molecular medicine*, vol. 7, no. 9, pp. 1–12, 5 2005. [Online]. Available: <http://www.ncbi.nlm.nih.gov/pubmed/15910695>
- [14] R. K. Chaganti and N. E. Lane, “Risk factors for incident osteoarthritis of the hip and knee,” pp. 99–104, 9 2011.
- [15] J. A. Martin and J. A. Buckwalter, “Aging, articular cartilage chondrocyte senescence and osteoarthritis,” pp. 257–264, 2002.
- [16] R. Plotnikoff, N. Karunamuni, E. Lytvynak, C. Penfold, D. Schopflocher, I. Imayama, S. T. Johnson, and K. Raine, “Osteoarthritis prevalence and modifiable factors: A population study Chronic Disease epidemiology,” *BMC Public Health*, vol. 15, no. 1, 11 2015.
- [17] D. T. Felson, “An update on the pathogenesis and epidemiology of osteoarthritis,” pp. 1–9, 2004.
- [18] D. T. Felson, Y. Zhang, M. T. Hannan, A. Naimark, B. N. Weissman, P. Aliabadi, and D. Levy, “The incidence and natural history of knee osteoarthritis in the elderly, the framingham osteoarthritis study,” *Arthritis & Rheumatism*, vol. 38, no. 10, pp. 1500–1505, 1995.
- [19] J. S. Schouten, F. A. Van Den Ouwehand, and H. A. Valkenburg, “A 12 year follow up study in the general population on prognostic factors of cartilage loss in osteoarthritis of the knee,” *Annals of the Rheumatic Diseases*, vol. 51, no. 8, pp. 932–937, 1992.
- [20] T. D. Spector, D. J. Hart, and D. V. Doyle, “Incidence and progression of osteoarthritis in women with unilateral knee disease in the general population: The effect of obesity,” *Annals of the Rheumatic Diseases*, vol. 53, no. 9, pp. 565–568, 1994.
- [21] “Hip Replacements - What to Expect & How to Prepare | NIAMS.” [Online]. Available: <https://www.niams.nih.gov/health-topics/hip-replacement-surgery/#tab-risk>
- [22] D. Metcalfe, “The pathophysiology of osteoporotic hip fracture.” *McGill journal of medicine : MJM : an international forum for the advancement of medical sciences by students*, vol. 11, no. 1, pp. 51–7, 1 2008. [Online]. Available: <http://www.ncbi.nlm.nih.gov/pubmed/18523524><http://www.ncbi.nlm.nih.gov/articlerender.fcgi?artid=PMC2322920>

- [23] G. A. Rodan, “Good hope for making osteoporosis a disease of the past,” *Osteoporosis International*, vol. 4, no. 1 Supplement, 1 1994.
- [24] World Health Organization (WHO), “Assessment of fracture risk and its application to screening for postmenopausal osteoporosis: Report of a WHO study group. WHO Technical Report Series, Report No. 843.” Tech. Rep., 1994.
- [25] K. Lippuner, M. Golder, and R. Greiner, “Epidemiology and direct medical costs of osteoporotic fractures in men and women in Switzerland.” *Osteoporosis international : a journal established as result of cooperation between the European Foundation for Osteoporosis and the National Osteoporosis Foundation of the USA*, vol. 16 Suppl 2, pp. S8–S17, 3 2005. [Online]. Available: <http://www.ncbi.nlm.nih.gov/pubmed/15378232>
- [26] B. L. Riggs and L. J. Melton, “The worldwide problem of osteoporosis: insights afforded by epidemiology.” *Bone*, vol. 17, no. 5 Suppl, pp. 505S–511S, 11 1995. [Online]. Available: <http://www.ncbi.nlm.nih.gov/pubmed/8573428>
- [27] T. Lindner, N. K. Kanakaris, B. Marx, A. Cockbain, G. Kontakis, and P. V. Giannoudis, “Fractures of the hip and osteoporosis: The role of bone substitutes,” *Journal of Bone and Joint Surgery - Series B*, vol. 91, no. 3, pp. 294–303, 3 2009.
- [28] M. J. Lespasio, N. Sodhi, and M. A. Mont, “Osteonecrosis of the Hip: A Primer,” 2019.
- [29] M. A. Mont and D. S. Hungerford, “Non-traumatic avascular necrosis of the femoral head.” *The Journal of bone and joint surgery. American volume*, vol. 77, no. 3, pp. 459–74, 3 1995. [Online]. Available: <http://www.ncbi.nlm.nih.gov/pubmed/7890797>
- [30] J. N. Lamb, C. Holton, P. O’Connor, and P. V. Giannoudis, “Avascular necrosis of the hip,” *BMJ*, p. l2178, 5 2019. [Online]. Available: <http://www.bmjjournals.org/lookup/doi/10.1136/bmj.l2178>
- [31] “Avascular Necrosis | Cedars-Sinai.” [Online]. Available: <https://www.cedars-sinai.org/health-library/diseases-and-conditions/a/avascular-necrosis.html>
- [32] K. L. Gebhard and H. I. Maibach, “Relationship between systemic corticosteroids and osteonecrosis.” *American journal of clinical dermatology*, vol. 2, no. 6, pp. 377–88, 2001. [Online]. Available: <http://www.ncbi.nlm.nih.gov/pubmed/11770392>
- [33] M. A. Mont, R. Pivec, S. Banerjee, K. Issa, R. K. Elmallah, and L. C. Jones, “High-Dose Corticosteroid Use and Risk of Hip Osteonecrosis: Meta-Analysis and Systematic Literature Review.” *The Journal of arthroplasty*, vol. 30, no. 9, pp. 1506–1512, 9 2015. [Online]. Available: <http://www.ncbi.nlm.nih.gov/pubmed/25900167>

- [34] K. Matsuo, T. Hirohata, Y. Sugioka, M. Ikeda, and A. Fukuda, “Influence of alcohol intake, cigarette smoking, and occupational status on idiopathic osteonecrosis of the femoral head.” *Clinical orthopaedics and related research*, no. 234, pp. 115–23, 9 1988. [Online]. Available: <http://www.ncbi.nlm.nih.gov/pubmed/3409564>
- [35] M. Kunstreich, S. Kummer, H.-J. Laws, A. Borkhardt, and M. Kuhlen, “Osteonecrosis in children with acute lymphoblastic leukemia.” *Haematologica*, vol. 101, no. 11, pp. 1295–1305, 2016. [Online]. Available: <http://www.ncbi.nlm.nih.gov/pubmed/27742768><http://www.ncbi.nlm.nih.gov/articlerender.fcgi?artid=PMC5394877>
- [36] “Total Hip Replacement Surgical Procedure.” [Online]. Available: <https://www.arthritis-health.com/surgery/hip-surgery/total-hip-replacement-surgical-procedure#targetText=A%20surgeon%20performing%20minimally%20invasive,cut%20through%20less%20soft%20tissue.&targetText=The%20surgeon%20dislocates%20the%20joint,off%20with%20a%20bone%20saw.>
- [37] “Total Hip Replacement - OrthoInfo - AAOS.” [Online]. Available: <https://orthoinfo.aaos.org/en/treatment/total-hip-replacement/>
- [38] S. J. M. Fischer, *100 Questions & Answers about Hip Replacements*. Jones and Bartlett Publishers, 2011.
- [39] R. Vaishya, M. Chauhan, and A. Vaish, “Bone cement,” pp. 157–163, 12 2013.
- [40] K. J. Bozic, A. F. Kamath, K. Ong, E. Lau, S. Kurtz, V. Chan, T. P. Vail, H. Rubash, and D. J. Berry, “Comparative Epidemiology of Revision Arthroplasty: Failed THA Poses Greater Clinical and Economic Burdens Than Failed TKA,” *Clinical Orthopaedics and Related Research*, vol. 473, no. 6, pp. 2131–2138, 6 2015.
- [41] J. T. Evans, J. P. Evans, R. W. Walker, A. W. Blom, M. R. Whitehouse, and A. Sayers, “How long does a hip replacement last? A systematic review and meta-analysis of case series and national registry reports with more than 15 years of follow-up,” *Lancet (London, England)*, vol. 393, no. 10172, pp. 647–654, 2 2019.
- [42] L. E. Murr, S. M. Gaytan, E. Martinez, F. Medina, and R. B. Wicker, “Next Generation Orthopaedic Implants by Additive Manufacturing Using Electron Beam Melting,” *International Journal of Biomaterials*, vol. 2012, p. 14, 2012. [Online]. Available: <http://www.pro-fit.de/>
- [43] “Types of Hip Replacement | Zimmer Biomet.” [Online]. Available: <https://www.zimmerbiomet.com/patients-caregivers/hip/about-hip-replacement.html>
- [44] S. Affatato, “Contemporary designs in total hip arthroplasty (THA),” in *Perspectives in Total Hip Arthroplasty*. Elsevier, 2014, pp. 46–64.

- [45] “General Information about Hip Implants | FDA.”
- [46] T. Scheerlinck and P.-P. Casteleyn, “The design features of cemented femoral hip implants,” *J Bone Joint Surg [Br]*, vol. 88, no. 11, pp. 88–1409, 2006.
- [47] R. B. Ruben, P. R. Fernandes, and J. Ao Folgado, “On the optimal shape of hip implants.” [Online]. Available: www.elsevier.com/locate/jbiomech
- [48] G. Tsikandylakis, M. Mohaddes, P. Cnudde, A. Eskelinen, J. Kärrholm, and O. Rolfson, “Head size in primary total hip arthroplasty,” *EFORT Open Reviews*, vol. 3, no. 5, pp. 225–231, 5 2018.
- [49] R. J. Tansey, G. L. Green, and F. S. Haddad, “Large diameter heads: Is bigger always better?” *Seminars in Arthroplasty*, vol. 26, no. 1, pp. 16–19, 3 2015.
- [50] S. Banerjee, R. Pivec, K. Issa, B. Kapadia, H. Khanuja, and M. Mont, “Large-Diameter Femoral Heads in Total Hip Arthroplasty: An Evidence-Based Review | MDedge Surgery,” pp. 506–512, 2014. [Online]. Available: <https://www.mdedge.com/surgery/article/88245/arthroplasty/joint-replacement/large-diameter-femoral-heads-total-hip>
- [51] G. Tsikandylakis, M. Mohaddes, P. Cnudde, A. Eskelinen, J. Kärrholm, and O. Rolfson, “Head size in primary total hip arthroplasty,” *EFORT Open Reviews*, vol. 3, no. 5, pp. 225–231, 5 2018.
- [52] S. M. Shah, W. L. Walter, S. M. Tai, M. F. Lorimer, and R. N. de Steiger, “Late Dislocations After Total Hip Arthroplasty: Is the Bearing a Factor?” *Journal of Arthroplasty*, vol. 32, no. 9, pp. 2852–2856, 9 2017.
- [53] H. Tanino, M. K. Harman, S. A. Banks, and W. A. Hodge, “Association between dislocation, impingement, and articular geometry in retrieved acetabular polyethylene cups.” *Journal of orthopaedic research : official publication of the Orthopaedic Research Society*, vol. 25, no. 11, pp. 1401–7, 11 2007. [Online]. Available: <http://www.ncbi.nlm.nih.gov/pubmed/17471491>
- [54] H. S. Hedia, A. A. A. Abdel-Shafi, and N. Fouda, “Shape optimization of metal backing for cemented acetabular cup,” Tech. Rep., 2000.
- [55] Z. M. Jin, D. Dowson, and J. Fisher, “A parametric analysis of the contact stress in ultra-high molecular weight polyethylene acetabular cups,” *Medical Engineering and Physics*, vol. 16, no. 5, pp. 398–405, 1994.
- [56] M. Al-Hamad, M. J. Le Duff, K. M. Takamura, and H. C. Amstutz, “Acetabular component thickness does not affect mid-term clinical results in hip resurfacing,” *Clinical Orthopaedics and Related Research*, vol. 472, no. 5, pp. 1528–1534, 2014.

- [57] M. J. Le Duff, C.-T. Wang, L. E. Wisk, K. B. Takamura, and H. C. Amstutz, “Benefits of thin-shelled acetabular components for metal-on-metal hip resurfacing arthroplasty,” *Journal of Orthopaedic Research*, vol. 28, no. 12, pp. 1665–1670, 12 2010. [Online]. Available: <http://doi.wiley.com/10.1002/jor.21176>
- [58] P. Goebel, D. Klüss, J. Wieding, R. Souffrant, H. Heyer, M. Sander, and R. Bader, “The influence of head diameter and wall thickness on deformations of metallic acetabular press-fit cups and UHMWPE liners: a finite element analysis.”
- [59] Y. Zhu, K. Chiu, and W. Tang, “Review Article: Polyethylene Wear and Osteolysis in Total Hip Arthroplasty,” *Journal of Orthopaedic Surgery*, vol. 9, no. 1, pp. 91–99, 6 2001. [Online]. Available: <http://journals.sagepub.com/doi/10.1177/230949900100900117>
- [60] C. Kenney, S. Dick, J. Lea, J. Liu, and N. A. Ebraheim, “A systematic review of the causes of failure of Revision Total Hip Arthroplasty,” pp. 393–395, 9 2019.
- [61] G. Bergmann, A. Bender, J. Dymke, G. Duda, and P. Damm, “Standardized Loads Acting in Hip Implants,” *PLOS ONE*, vol. 11, no. 5, p. e0155612, 5 2016. [Online]. Available: <https://dx.plos.org/10.1371/journal.pone.0155612>
- [62] S. E. Graves, D. Davidson, L. Ingerson, P. Ryan, E. C. Griffith, B. F. McDermott, H. J. McElroy, and N. L. Pratt, “The Australian Orthopaedic Association National Joint Replacement Registry,” *Medical Journal of Australia*, vol. 180, no. 5 SUPPL., 3 2004.
- [63] G. Garellick, C. Rogmark, J. Kärrholm, and O. Rolfson, “Swedish Hip Arthroplasty Register Annual Report 2012.” [Online]. Available: www.shpr.se.
- [64] “HIP INSTABILITY: CAUSES AND MANAGEMENT | Orthopaedic Proceedings.” [Online]. Available: <https://online.boneandjoint.org.uk/doi/abs/10.1302/1358-992X.2018.10.041>
- [65] M. J. DeRogatis, E. Wintermeyer, T. R. Sperring, and P. S. Issack, “Modular Fluted Titanium Stems in Revision Hip Arthroplasty,” *The Journal of Bone and Joint Surgery*, vol. 101, no. 8, pp. 745–754, 4 2019. [Online]. Available: <http://insights.ovid.com/crossref?an=00004623-201904170-00011>
- [66] “Modular Dual Mobility | Stryker.” [Online]. Available: <https://www.stryker.com/us/en/joint-replacement/products/modular-dual-mobility.html>
- [67] I. De Martino, G. K. Triantafyllopoulos, P. K. Sculco, and T. P. Sculco, “Dual mobility cups in total hip arthroplasty,” *World Journal of Orthopaedics*, vol. 5, no. 3, pp. 180–187, 2014.

- [68] A. Combes, H. Migaud, J. Girard, A. Duhamel, and M. H. Fessy, “Low rate of dislocation of dual-mobility cups in primary total hip arthroplasty,” in *Clinical Orthopaedics and Related Research*, vol. 471, no. 12. Springer New York LLC, 2013, pp. 3891–3900.
- [69] P. J. Duwelius, B. Burkhardt, C. Carnahan, G. Branam, L. M. Ko, Y. Wu, C. Froemke, L. Wang, and G. Grunkemeier, “Modular versus nonmodular neck femoral implants in primary total hip arthroplasty: Which is better?” *Clinical Orthopaedics and Related Research*, vol. 472, no. 4, pp. 1240–1245, 2014.
- [70] A. B. Shaik and D. Sarkar, “Dynamic Analysis and Life Estimation of the Artificial Hip Joint Prosthesis,” 2020, pp. 265–274.
- [71] “Falls and vehicle collisions top causes of injury hospitalizations for seniors | CIHI.” [Online]. Available: <https://www.cihi.ca/en/falls-and-vehicle-collisions-top-causes-of-injury-hospitalizations-for-seniors>
- [72] A. F. Mavrogenis, R. Dimitriou, J. Parvizi, and G. C. Babis, “Biology of implant osseointegration,” *Journal of Musculoskeletal Neuronal Interactions*, vol. 9, no. 2, pp. 61–71, 2009. [Online]. Available: <http://www.ismni.org/jmni/pdf/36/01MAVROGENIS.pdf%0Ahttps://www.scopus.com/inward/record.uri?eid=2-s2.0-68849129955&partnerID=40&md5=d93099cf0d39b2d130d42b539f72ec28>
- [73] “THE GLOSSARY OF PROSTHODONTIC TERMS,” *The Journal of Prosthetic Dentistry*, vol. 94, no. 1, pp. 10–92, 2005.
- [74] C. Y. Hu and T. R. Yoon, “Recent updates for biomaterials used in total hip arthroplasty,” *Biomaterials Research*, vol. 22, no. 1, pp. 1–12, 2018.
- [75] M. R. Dharme, A. M. Kuthe, and S. W. Dahake, “Comparison of fatigue analysis of hip joint implant for stainless steel, cobalt chrome alloys and titanium alloys,” *Trends in Biomaterials and Artificial Organs*, vol. 27, no. 2, pp. 58–61, 2013.
- [76] M. Niinomi and M. Nakai, “Titanium-based biomaterials for preventing stress shielding between implant devices and bone,” *International Journal of Biomaterials*, vol. 2011, 2011.
- [77] S. G. Ghalme, A. Mankar, and Y. Bhalerao, “Biomaterials in Hip Joint Replacement,” *International Journal of Materials Science and Engineering*, vol. 4, no. 2, pp. 113–125, 2016. [Online]. Available: <http://www.ijmse.net/uploadfile/2016/0715/20160715041827481.pdf>
- [78] R. Singh and N. B. Dahotre, “Corrosion degradation and prevention by surface modification of biometallic materials,” *Journal of Materials Science: Materials in Medicine*, vol. 18, no. 5, pp. 725–751, 2007.

- [79] N. Sumitomo, K. Noritake, T. Hattori, K. Morikawa, S. Niwa, K. Sato, and M. Niinomi, “Experiment study on fracture fixation with low rigidity titanium alloy: Plate fixation of tibia fracture model in rabbit,” *Journal of Materials Science: Materials in Medicine*, vol. 19, no. 4, pp. 1581–1586, 2008.
- [80] M. A. Khan, R. L. Williams, and D. F. Williams, “In-vitro corrosion and wear of titanium alloys in the biological environment,” vol. 17, pp. 2117–2126, 1996. [Online]. Available: papers3://publication/uuid/8F2A93E8-2634-48C5-9A67-F3E6AF1268BC
- [81] J. E. González and J. C. Mirza-Rosca, “Study of the corrosion behavior of titanium and some of its alloys for biomedical and dental implant applications,” *Journal of Electroanalytical Chemistry*, vol. 471, no. 2, pp. 109–115, 1999.
- [82] I. Gurappa, “Characterization of different materials for corrosion resistance under simulated body fluid conditions,” vol. 49, pp. 73–79, 2002.
- [83] N. D. Tomashov, G. P. Chernova, Y. S. Ruscol, and G. A. Ayuyan, “The passivation of alloys on titanium bases,” *Electrochimica Acta*, vol. 19, no. 4, pp. 159–172, 1974.
- [84] F. Matassi, A. Botti, L. Sirleo, C. Carulli, and M. Innocenti, “Porous metal for orthopedics implants,” *Clinical Cases in Mineral and Bone Metabolism*, vol. 10, no. 2, pp. 111–115, 2013.
- [85] V. K. Balla, S. Bodhak, S. Bose, and A. Bandyopadhyay, “Porous tantalum structures for bone implants: Fabrication, mechanical and in vitro biological properties,” *Acta Biomaterialia*, vol. 6, no. 8, pp. 3349–3359, 2010. [Online]. Available: <http://dx.doi.org/10.1016/j.actbio.2010.01.046>
- [86] I. Landor, P. Vavrik, A. Sosna, D. Jahoda, H. Hahn, and M. Daniel, “Hydroxyapatite porous coating and the osteointegration of the total hip replacement,” *Archives of Orthopaedic and Trauma Surgery*, vol. 127, no. 2, pp. 81–89, 2007.
- [87] J. M. Gomez-Vega, E. Saiz, and A. P. Tomsia, “Glass-based coatings for titanium implant alloys,” *Journal of Biomedical Materials Research*, vol. 46, no. 4, pp. 549–559, 1999.
- [88] L. Sun, C. C. Berndt, K. A. Gross, and A. Kucuk, “Material Fundamentals and Clinical Performance of Plasma-Sprayed Hydroxyapatite Coatings: A Review,” *John Wiley & Sons, Inc.*, pp. 570–592, 2001.
- [89] S. R. Knight, R. Aujla, and S. P. Biswas, “Total Hip Arthroplasty - over 100 years of operative history,” *Orthopaedic Reviews*, vol. 3, pp. 2–4, 2011.
- [90] A. Bonnefoy-Mazure and S. Armand, “Normal gait,” in *Orthopedic Management of Children with Cerebral Palsy: A Comprehensive Approach*, 2015.

- [91] P. J. Mansfield and D. A. Neumann, *Essentials of Kinesiology for the Physical Therapist Assistant*. Elsevier, 2019.
- [92] J. L. McCrory, S. C. White, and R. M. Lifeso, “Vertical ground reaction forces: Objective measures of gait following hip arthroplasty,” *Gait and Posture*, vol. 14, no. 2, pp. 104–109, 2001.
- [93] X. Xu, R. W. McGorry, L. S. Chou, J. h. Lin, and C. c. Chang, “Accuracy of the Microsoft Kinect™ for measuring gait parameters during treadmill walking,” *Gait and Posture*, vol. 42, no. 2, pp. 145–151, 7 2015.
- [94] G. Bovi, M. Rabuffetti, P. Mazzoleni, and M. Ferrarin, “A multiple-task gait analysis approach: Kinematic, kinetic and EMG reference data for healthy young and adult subjects,” *Gait and Posture*, vol. 33, no. 1, pp. 6–13, 1 2011.
- [95] D. A. Winter, Ed., *Biomechanics and {Motor} {Control} of {Human} {Movement}*, 4th ed. John Wiley & Sons, Inc., 2009.
- [96] D. A. Winter, “Biomechanics of normal and pathological gait: Implications for understanding human locomotor control,” *Journal of Motor Behavior*, vol. 21, no. 4, pp. 337–355, 1989.
- [97] M. L. Beaulieu, M. Lamontagne, and P. E. Beaulé, “Lower limb biomechanics during gait do not return to normal following total hip arthroplasty,” *Gait and Posture*, vol. 32, no. 2, pp. 269–273, 6 2010.
- [98] M. Perron, F. Malouin, H. Moffet, and B. J. McFadyen, “Three-dimensional gait analysis in women with a total hip arthroplasty,” *Clinical Biomechanics*, vol. 15, no. 7, pp. 504–515, 8 2000.
- [99] G. Bergmann, G. Deuretzbacher, M. Heller, F. Graichen, A. Rohlmann, J. Strauss, and G. Duda, “Hip contact forces and gait patterns from routine activities,” *Journal of Biomechanics*, vol. 34, no. 7, pp. 859–871, 7 2001. [Online]. Available: <https://linkinghub.elsevier.com/retrieve/pii/S0021929001000409>
- [100] G. Bergmann, F. Graichen, and A. Rohlmann, “Hip joint contact forces during stumbling,” *Langenbeck's Archives of Surgery*, vol. 389, no. 1, pp. 53–59, 2 2004. [Online]. Available: <http://link.springer.com/10.1007/s00423-003-0434-y>
- [101] M. Heller, G. Bergmann, J.-P. Kassi, L. Claes, N. Haas, and G. Duda, “Determination of muscle loading at the hip joint for use in pre-clinical testing,” *Journal of Biomechanics*, vol. 38, no. 5, pp. 1155–1163, 5 2005. [Online]. Available: <https://linkinghub.elsevier.com/retrieve/pii/S002192900400260X>
- [102] G. Lenaerts, W. Bartels, F. Gelaude, M. Mulier, A. Spaepen, G. Van der Perre, and I. Jonkers, “Subject-specific hip geometry and hip joint centre location affects calculated contact forces at the hip during gait,” *Journal*

- of Biomechanics*, vol. 42, no. 9, pp. 1246–1251, 6 2009. [Online]. Available: <https://linkinghub.elsevier.com/retrieve/pii/S0021929009001420>
- [103] “[Levangie] Joint Structure and function (5th ed, 2011).pdf.”
 - [104] “Range of Motion - an overview | ScienceDirect Topics.” [Online]. Available: <https://www.sciencedirect.com/topics/immunology-and-microbiology/range-of-motion>
 - [105] S. Hudson, “Rehabilitation of the cat,” in *Feline Orthopedic Surgery and Musculoskeletal Disease*. Elsevier Inc., 2009, pp. 221–235.
 - [106] J. A. D’antonio and M. Dietrich, “0*[^] BIOLOX® Symposium Proceedings Edited by,” Tech. Rep.
 - [107] J. G. Konin and B. Jessee, “Range of motion and flexibility,” in *Physical Rehabilitation of the Injured Athlete*. Elsevier Inc., 2012, pp. 74–88.
 - [108] D. C. Boone and S. P. Azen, “Normal range of motion of joints in male subjects.” *The Journal of bone and joint surgery. American volume*, vol. 61, no. 5, pp. 756–9, 7 1979. [Online]. Available: <http://www.ncbi.nlm.nih.gov/pubmed/457719>
 - [109] S. Svenningsen, T. Terjesen, M. Auflern, and V. Berg, “Acta Orthopaedica Scandinavica Hip motion related to age and sex,” 2009. [Online]. Available: <https://www.tandfonline.com/action/journalInformation?journalCode=hort20>
 - [110] “Joint motion: Method of measuring and recording. Published for the British Orthopaedic Association. Pp. 87. 1966. Edinburgh & London: E. & S. Livingstone. 7s. 6d,” *British Journal of Surgery*, vol. 53, no. 6, pp. 562–562, 6 1966.
 - [111] A. Roaas and G. B. J. Andersson, “Normal Range of Motion of the Hip, Knee and Ankle Joints in Male Subjects, 30-40 Years of Age,” *Acta Orthopaedica Scandinavica*, vol. 53, no. 2, pp. 205–208, 1982. [Online]. Available: <https://www.tandfonline.com/action/journalInformation?journalCode=hort20>
 - [112] A. I. Kapandji, *The Physiology of the Joints, The Upper limb*. Churchill Livingstone, 2007, vol. One.
 - [113] K. E. Roach and T. P. Miles, “Normal hip and knee active range of motion: The relationship to age,” *Physical Therapy*, vol. 71, no. 9, pp. 656–665, 1991.
 - [114] M. J. Le Duff, L. E. Wisk, and H. C. Amstutz, “Range of motion after stemmed total hip arthroplasty and hip resurfacing - a clinical study.” *Bulletin of the NYU hospital for joint diseases*, vol. 67, no. 2, pp. 177–81, 2009. [Online]. Available: <http://www.ncbi.nlm.nih.gov/pubmed/19583550>
 - [115] E. Trudelle-Jackson, R. Emerson, and S. Smith, “Outcomes of Total Hip Arthroplasty: A Study of Patients One Year Postsurgery,” Tech. Rep., 2002. [Online]. Available: www.jospt.org

- [116] F. Blaisdell and C. P. Anthony, “Structure and Function of the Body,” *The American Journal of Nursing*, vol. 69, no. 5, p. 1075, 1969.
- [117] “SimTK: OpenSim: Project Home.” [Online]. Available: <https://simtk.org/projects/opensim>
- [118] D. R. Pedersen, R. A. Brand, and D. T. Davy, “Pelvic muscle and acetabular contact forces during gait,” *Journal of Biomechanics*, vol. 30, no. 9, pp. 959–965, 9 1997.
- [119] R. Dattani, “Femoral osteolysis following total hip replacement,” pp. 312–316, 5 2007.
- [120] L. JMS, “Total Hip Replacement: Tensile Stress in Bone Cement is influenced by Cement Mantle Thickness, Acetabular Size, Bone Quality, and Body Mass Index,” *Journal of Computer Science & Systems Biology*, vol. 7, no. 3, 2014.
- [121] “G7 ACE TABULAR SYSTEM Surgical Technique,” Tech. Rep.
- [122] Zimmer and Inc, “Zimmer® M/L Taper Hip Prosthesis Surgical Technique 97-7711-202-00,” Tech. Rep.
- [123] N. Taniguchi, T. Jinno, R. Takada, D. Koga, T. Ando, A. Okawa, and H. Haro, “Do screws and screw holes affect osteolysis in cementless cups using highly crosslinked polyethylene? A 7 to 10-year follow-up case-control study,” *Orthopaedics and Traumatology: Surgery and Research*, vol. 104, no. 3, pp. 307–315, 5 2018.
- [124] R. A. Gallen, R. J. Khan, S. J. Haebich, S. H. Karamfiles, and H. Khan, “Solid Cup vs Cluster Hole in Total Hip Arthroplasty: A 10-Year Randomized Control Trial,” *Journal of Arthroplasty*, vol. 33, no. 4, pp. 1113–1119, 4 2018.
- [125] W. G. Blakeney, H. Khan, and R. J. Khan, “Cluster hole versus solid cup in total hip arthroplasty: A randomized control trial,” *Journal of Arthroplasty*, vol. 30, no. 2, pp. 223–229, 2 2015.
- [126] T. P. Schmalzried, “The role of acetabular component screw holes and/or screws in the development of pelvic osteolysis,” *Proceedings of the Institution of Mechanical Engineers, Part H: Journal of Engineering in Medicine*, vol. 213, no. 2, pp. 147–153, 1999.
- [127] “Taperloc Complete Hip System Surgical Technique,” Tech. Rep.
- [128] “Titanium & Titanium Alloy for Medical Applications | DAIDO STEEL.” [Online]. Available: <https://www.daido.co.jp/en/products/titanium/medical.html>
- [129] M. Saini, “Implant biomaterials: A comprehensive review,” *World Journal of Clinical Cases*, vol. 3, no. 1, p. 52, 2015.

- [130] B. Vamsi Krishna, W. Xue, S. Bose, and A. Bandyopadhyay, “Functionally graded Co-Cr-Mo coating on Ti-6Al-4V alloy structures,” *Acta Biomaterialia*, vol. 4, no. 3, pp. 697–706, 5 2008.
- [131] F. J. Kummer and R. M. Rose, “Corrosion of titanium/cobalt-chromium alloy couples,” *Journal of Bone and Joint Surgery - Series A*, vol. 65, no. 8, pp. 1125–1126, 1983.
- [132] L. Zagra and E. Gallazzi, “Bearing surfaces in primary total hip arthroplasty,” *EFORT Open Reviews*, vol. 3, no. 5, pp. 217–224, 5 2018.
- [133] J. C. Fox and T. M. Keaveny, “Trabecular eccentricity and bone adaptation,” *Journal of Theoretical Biology*, vol. 212, no. 2, pp. 211–221, 9 2001.
- [134] S. Arabnejad, B. Johnston, M. Tanzer, and D. Pasini, “Fully porous 3D printed titanium femoral stem to reduce stress-shielding following total hip arthroplasty,” *Journal of Orthopaedic Research*, vol. 35, no. 8, pp. 1774–1783, 8 2017.
- [135] S. Peng, Z. Li, L. Zou, W. Liu, C. Liu, and D. J. McClements, “Improving curcumin solubility and bioavailability by encapsulation in saponin-coated curcumin nanoparticles prepared using a simple pH-driven loading method,” *Food and Function*, vol. 9, no. 3, pp. 1829–1839, 3 2018.
- [136] S. An, F. Han, Y. Hu, Y. Liu, J. Li, and L. Wang, “Curcumin Inhibits Polyethylene-Induced Osteolysis via Repressing NF- κ B Signaling Pathway Activation,” *Cellular Physiology and Biochemistry*, vol. 50, no. 3, pp. 1100–1112, 2018. [Online]. Available: <https://www.karger.com/Article/FullText/494537>
- [137] R. S. Virk, M. A. Ur Rehman, M. A. Munawar, D. W. Schubert, W. H. Goldmann, J. Dusza, and A. R. Boccaccini, “Curcumin-containing orthopedic implant coatings deposited on poly-ether-ether-ketone/bioactive glass/hexagonal boron nitride layers by electrophoretic deposition,” *Coatings*, vol. 9, no. 9, 9 2019.
- [138] C. L. Romanò, K. Malizos, N. Capuano, R. Mezzoprete, M. D'Arienzo, C. Van Der Straeten, S. Scarponi, and L. Drago, “Does an Antibiotic-Loaded Hydrogel Coating Reduce Early Post-Surgical Infection After Joint Arthroplasty?” *Journal of Bone and Joint Infection*, vol. 1, pp. 34–41, 8 2016.
- [139] “DAC® | Defensive Antibacterial Coating.” [Online]. Available: <http://www.dac-coating.com/>
- [140] S. B. Mirza, D. G. Dunlop, S. S. Panesar, S. G. Naqvi, S. Gangoo, and S. Salih, “Basic Science Considerations in Primary Total Hip Replacement Arthroplasty,” *The Open Orthopaedics Journal*, vol. 4, no. 1, pp. 169–180, 5 2010.

- [141] L. Stathokostas, M. W. McDonald, R. M. Little, and D. H. Paterson, “Flexibility of older adults aged 55-86 years and the influence of physical activity,” *Journal of Aging Research*, vol. 2013, 2013.
- [142] “Ultimate Strength of the Human Femur – Body Physics: Motion to Metabolism.” [Online]. Available: <https://openoregon.pressbooks.pub/bodyphysics/chapter/stress-and-strain-on-the-body/>
- [143] J. M. Struemph, A. C. M. Chong, and P. H. Wooley, “Evaluation of Different Experience Levels of Orthopaedic Residents Effect on Polymethylmethacrylate (PMMA) Bone Cement Mechanical Properties.” *The Iowa orthopaedic journal*, vol. 35, pp. 193–8, 2015. [Online]. Available: <http://www.ncbi.nlm.nih.gov/pubmed/26361465><http://www.ncbi.nlm.nih.gov/articlerender.fcgi?artid=PMC4492133>
- [144] “Properties: Titanium Alloys - Ti6Al7Nb Properties and Applications.” [Online]. Available: https://www_azom_com/properties.aspx?ArticleID=2064
- [145] M. I. Ridzwan, S. Shuib, A. Y. Hassan, A. A. Shokri, and M. N. Mohammad Ibrahim, “Problem of stress shielding and improvement to the hip implant designs: A review,” pp. 460–467, 4 2007.
- [146] “Friction and Wear Data Bank 15.1 Introduction 15.2 Sources of Data 15.3 Materials Found in Data Bank Metals for Fluid (Oil) Film Bearings • Porous Metals • Plastics • Carbon-Graphites • Miscellaneous Nonmetallic Materials • Materials under Abrasive Wear 1,” Tech. Rep., 2001.
- [147] O. V. Kovalevskaya, Y. I. Gordeev, and [U+FFF] [U+FFF] Abkaryan, “POLYMER COMPOSITE MATERIALS BASED ON ULTRA HIGH MOLECULAR WEIGHT POLYETHYLENE MATRIX FILLED BY ALUMINUM OXIDE POWDERS,” Tech. Rep.
- [148] T. Akahori, M. Niinomi, and A. Suzuki, “Improvement in Mechanical Properties of Dental Cast Ti-6Al-7Nb by Thermochemical Processing,” Tech. Rep.
- [149] “ASTM Compass.” [Online]. Available: https://compass.astm.org/EDIT/html_annot.cgi?F2068+15
- [150] “ISO - ISO 7206-10:2018 - Implants for surgery — Partial and total hip-joint prostheses — Part 10: Determination of resistance to static load of modular femoral heads.” [Online]. Available: <https://www.iso.org/standard/71145.html>
- [151] G. Bergmann, A. Bender, J. Dymke, G. Duda, and P. Damm, “Standardized Loads Acting in Hip Implants,” *PLOS ONE*, vol. 11, no. 5, p. e0155612, 5 2016. [Online]. Available: <https://dx.plos.org/10.1371/journal.pone.0155612>

- [152] “Cobalt Chromium Molybdenum Alloy | AMERICAN ELEMENTS ®.” [Online]. Available: <https://www.americanelements.com/cobalt-chromium-molybdenum-alloy>
- [153] R. V. Marrey, R. Burgermeister, R. B. Grishaber, and R. O. Ritchie, “Fatigue and life prediction for cobalt-chromium stents: A fracture mechanics analysis,” *Biomaterials*, vol. 27, 2006. [Online]. Available: www.elsevier.com/locate/biomaterials
- [154] A. Eriksson, G. Tibert, J. H. Zhao, S. Nagao, and Z. L. Zhang, “23rd Nordic Seminar on Computational Mechanics NSCM-23 THE EFFECT OF CROSSLINKED AND BRANCHED POLYETHYLENE MOLECULES ON THE THERMO-MECHANICAL PROPERTIES,” Tech. Rep.
- [155] E. Oral, S. D. Christensen, A. S. Malhi, K. K. Wannomae, and O. K. Muratoglu, “Wear Resistance and Mechanical Properties of Highly Cross-linked, Ultrahigh-Molecular Weight Polyethylene Doped With Vitamin E,” *Journal of Arthroplasty*, vol. 21, no. 4, pp. 580–591, 6 2006.
- [156] R. R. Khasawneh, M. Z. Allouh, and E. Abu-El-rub, “Measurement of the quadriceps(Q)angle with respect to various body parameters in young Arab population,” *PLoS ONE*, vol. 14, no. 6, 6 2019.
- [157] E. R. Henderson, G. A. Marulanda, D. Cheong, H. T. Temple, and G. D. Letson, “Hip abductor moment arm - a mathematical analysis for proximal femoral replacement,” *Journal of Orthopaedic Surgery and Research*, vol. 6, no. 1, 1 2011.

Appendices

A Anthropometric Data

A.1 Winter's Anthropometric Data

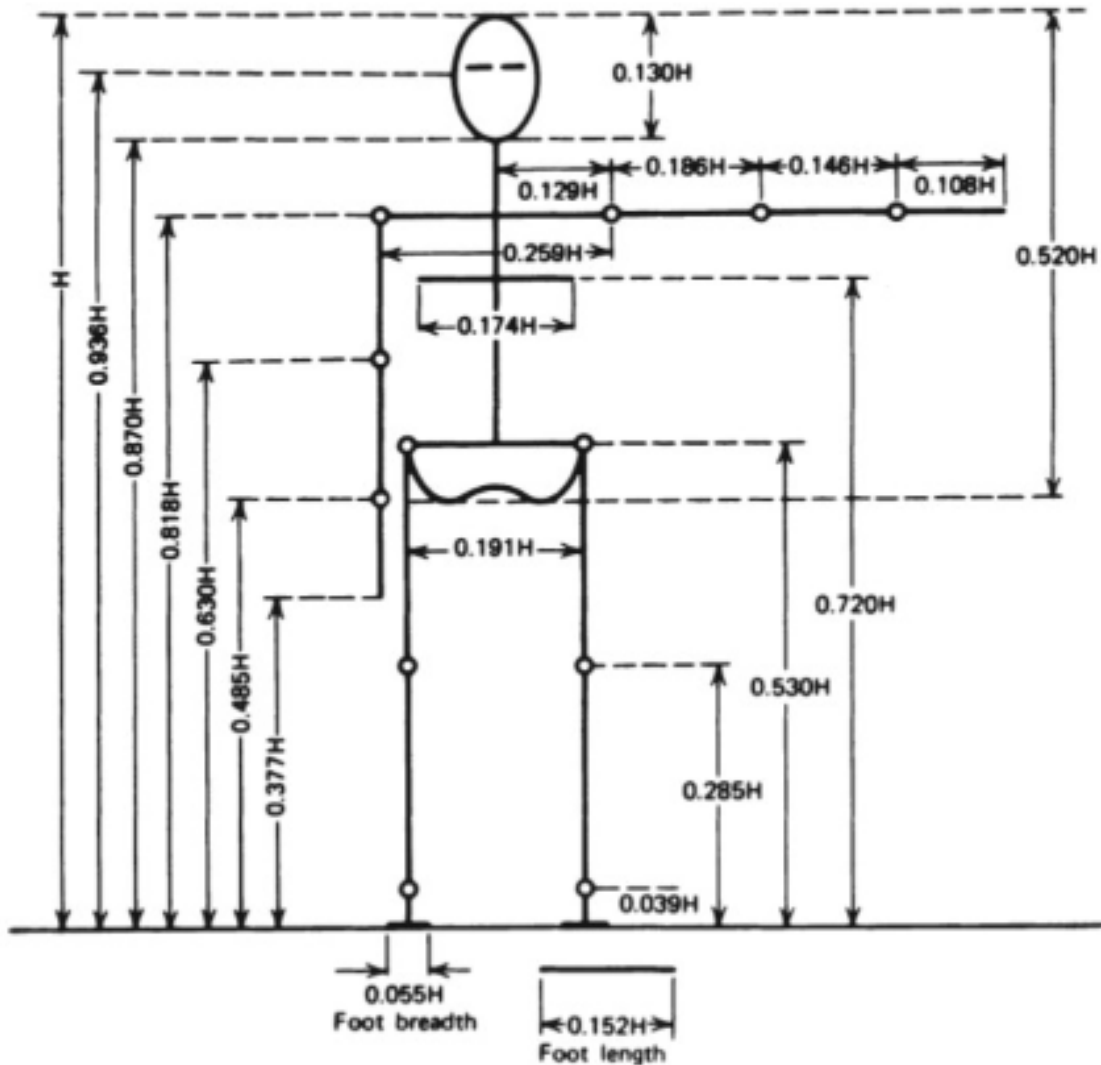


Figure A.33: Classical anthropometric model from Drillis and Contini, 1964 - via Winter, 2009 [95]

TABLE 4.1 Anthropometric Data

Segment	Definition	Segment Weight/Total Body Weight	Center of Mass/Segment Length		Radius of Gyration/Segment Length			Density
			Proximal	Distal	C of G	Proximal	Distal	
Hand	Wrist axis/knuckle II middle finger	0.006 M	0.506	0.494 P	0.297	0.587	0.577 M	1.16
Forearm	Elbow axis/ulnar styloid	0.016 M	0.430	0.570 P	0.303	0.526	0.647 M	1.13
Upper arm	Glenohumeral axis/elbow axis	0.028 M	0.436	0.564 P	0.322	0.542	0.645 M	1.07
Forearm and hand	Elbow axis/ulnar styloid	0.022 M	0.682	0.318 P	0.468	0.827	0.565 P	1.14
Total arm	Glenohumeral joint/ulnar styloid	0.050 M	0.530	0.470 P	0.368	0.645	0.596 P	1.11
Foot	Lateral malleolus/head metatarsal II	0.0145 M	0.50	0.50 P	0.475	0.690	0.690 P	1.10
Leg	Femoral condyles/medial malleolus	0.0465 M	0.433	0.567 P	0.302	0.528	0.643 M	1.09
Thigh	Greater trochanter/femoral condyles	0.100 M	0.433	0.567 P	0.323	0.540	0.653 M	1.05
Foot and leg	Femoral condyles/medial malleolus	0.061 M	0.606	0.394 P	0.416	0.735	0.572 P	1.09
Total leg	Greater trochanter/medial malleolus	0.161 M	0.447	0.553 P	0.326	0.560	0.650 P	1.06
Head and neck	C7-T1 and 1st rib/ear canal	0.081 M	1.000	— PC	0.495	0.116	— PC	1.11
Shoulder mass	Sternoclavicular joint/glenohumeral axis	—	0.712	0.288	—	—	—	1.04
Thorax	C7-T1/T12-L1 and diaphragm*	0.216 PC	0.82	0.18	—	—	—	0.92
Abdomen	T12-L1/L4-L5*	0.139 LC	0.44	0.56	—	—	—	—
Pelvis	L4-L5/greater trochanter*	0.142 LC	0.105	0.895	—	—	—	—
Thorax and abdomen	C7-T1/L4-L5*	0.355 LC	0.63	0.37	—	—	—	—
Abdomen and pelvis	T12-L1/greater trochanter*	0.281 PC	0.27	0.73	—	—	—	1.01
Trunk	Greater trochanter/glenohumeral joint*	0.497 M	0.50	0.50	—	—	—	1.03
Trunk head neck	Greater trochanter/glenohumeral joint*	0.578 MC	0.66	0.34 P	0.503	0.830	0.607 M	—
Head, arms, and trunk (HAT)	Greater trochanter/glenohumeral joint*	0.678 MC	0.626	0.374 PC	0.496	0.798	0.621 PC	—
HAT	Greater trochanter/mid rib	0.678	1.142	—	0.903	1.456	—	—

*NOTE: These segments are presented relative to the length between the greater trochanter and the glenohumeral joint.

Source Codes: M, Dempster via Miller and Nelson; *Biomechanics of Sport*, Lea and Febiger, Philadelphia, 1973. P, Dempster via Plagenhoef; *Patterns of Human Motion*, Prentice-Hall, Inc. Englewood Cliffs, NJ, 1971. L, Dempster via Plagenhoef from living subjects; *Patterns of Human Motion*, Prentice-Hall, Inc., Englewood Cliffs, NJ, 1971. C, Calculated.

A.2 Elderly Anthropometric Data

	Age group	n	Mean	SD	Centile					
					5	10	25	50	75	95
Weight (kg)†‡	65–69	466	74.6 ^a	11.2	58	61	67	74	81	89
	70–74	451	74.4 ^a	11.9	57	60	66	73	81	91
	75–79	392	69.5 ^b	10.7	53	55	62	69	77	84
	80–84	365	66.7 ^c	10.7	50	53	59	66	74	80
All men	1674	72.6*	10.7*	54	57	64	71	78	86	92
Height (cm)†‡	65–69	469	167.1 ^a	7.5	155	157	162	167	172	177
	70–74	457	166.3 ^a	6.4	156	159	162	166	170	175
	75–79	407	163.8 ^b	6.6	153	156	159	163	168	172
	80–84	384	162.7 ^c	7.2	151	153	158	162	168	175
All men	1717	165.7*	6.7*	154	156	160	165	170	175	177
BMI†‡ (kg/m ²)	65–69	465	26.8 ^a	4.2	21.2	22.3	24.3	26.6	28.7	31.2
	70–74	448	27.0 ^a	3.9	20.8	22.2	24.3	26.5	29.1	32.0
	75–79	391	26.0 ^b	3.6	20.4	21.4	23.4	26.0	28.2	31.2
	80–84	362	25.2 ^c	3.6	19.6	20.8	23.0	25.0	27.4	29.6
All men	1666	26.4*	3.7*	20.7	21.7	23.7	26.0	28.4	31.2	32.7
Waist circumference (cm)‡	65–69	467	98.1 ^a	10.2	82	85	92	98	104	111
	70–74	458	98.5 ^a	11.1	81	85	92	98	105	112
	75–79	409	96.4 ^b	10.7	79	83	89	97	103	110
	80–84	395	94.8 ^c	11.3	77	82	88	95	102	108
All men	1729	97.5*	9.9*	80	84	90	97	104	110	115
Hip circumference (cm)‡	65–69	467	100.6 ^a	8.4	89	92	96	100	105	111
	70–74	458	101.0 ^a	9.6	89	92	96	101	106	112
	75–79	409	99.6 ^b	8.9	87	90	94	100	105	110
	80–84	387	98.3 ^b	9.6	86	89	94	98	104	109
All men	1721	100.2*	8.3*	88	91	95	100	105	110	115
Waist:hip ratio†‡	65–69	466	0.97 ^a	0.05	0.88	0.90	0.93	0.97	1.01	1.04
	70–74	456	0.97 ^a	0.06	0.88	0.90	0.94	0.97	1.00	1.04
	75–79	404	0.96 ^b	0.05	0.87	0.90	0.93	0.96	1.00	1.03
	80–84	384	0.95 ^c	0.06	0.86	0.88	0.92	0.95	0.99	1.02
All men	1710	0.97*	0.05*	0.87	0.89	0.93	0.96	1.00	1.03	1.05

	Age group	<i>n</i>	Mean	SD	Centile						
					5	10	25	50	75	90	95
Weight (kg)†‡	65–69	418	66.2 ^a	12.0	49	52	58	65	73	81	90
	70–74	370	64.8 ^a	12.5	46	51	55	63	73	81	85
	75–79	361	61.1 ^b	10.6	45	48	54	61	68	76	79
	80–84	313	60.0 ^b	11.7	42	46	52	59	67	77	80
	All women	1462	63.8*	13.1*	45	49	55	62	71	79	84
Height (cm)†‡	65–69	436	154.1 ^a	6.7	143	146	150	154	159	163	165
	70–74	379	152.3 ^b	6.5	142	144	148	152	157	160	163
	75–79	373	150.6 ^c	6.4	141	143	146	151	155	159	161
	80–84	329	149.3 ^d	7.00	138	141	144	149	154	158	160
	All women	1517	152.2*	7.5*	141	143	147	152	156	160	163
BMI†‡ (kg/m ²)	65–69	417	28.0 ^a	5.2	21.0	22.1	24.4	27.3	30.6	35.2	37.4
	70–74	368	27.9 ^a	5.0	20.4	21.9	24.3	27.4	31.2	33.8	36.0
	75–79	361	27.1 ^b	5.2	20.0	21.2	23.7	26.5	29.9	32.4	34.4
	80–84	308	27.1 ^b	5.8	18.9	20.4	23.5	26.7	30.1	33.4	35.6
	All women	1454	27.6*	5.7*	20.1	21.5	24	27	30	34	36.4
Waist circumference (cm)	65–69	440	97.2 ^a	13.2	75.5	80	89	97	105.5	114	121.5
	70–74	389	97.4 ^a	12.9	76	80	89	98	106	114	119
	75–79	375	96.2 ^a	12.4	75	80	88	96	104	112	117
	80–84	346	96.5 ^a	12.8	75	80	89	97	105	113	117
	All women	1550	96.9*	14.1*	75	80	88	97	106	113	118
Hip circumference (cm)†‡	65–69	440	104.5 ^a	11.5	88	91	97	103	110	119	125
	70–74	390	104.0 ^a	10.7	88	92	96	103	111	117.5	123
	75–79	373	102.3 ^b	10.4	87	90	96	101	109	116	122
	80–84	347	101.5 ^b	11.4	85	89	95	102	108	116	120
	All women	1550	103.4*	12.1*	87	90	96	102	110	117	123
Waist:hip ratio†	65–69	438	0.93 ^a	0.06	0.80	0.83	0.88	0.93	0.97	1.01	1.04
	70–74	389	0.93 ^a	0.07	0.81	0.84	0.89	0.93	0.98	1.02	1.04
	75–79	372	0.94 ^a	0.07	0.82	0.85	0.90	0.93	0.98	1.02	1.04
	80–84	345	0.95 ^b	0.06	0.83	0.86	0.90	0.95	0.99	1.03	1.05
	All women	1544	0.94*	0.08*	0.81	0.84	0.89	0.94	0.98	1.02	1.04

B Static Force Calculations

Frontal Plane: Ankle:

$$\begin{aligned}
 \sum F_z &= 0 \\
 GRF_z - F_{az} &= 0 \\
 F_{az} &= GRF_z \\
 F_{az} &= 40.02N
 \end{aligned} \tag{15}$$

$$\begin{aligned}
 \sum F_y &= 0 \\
 GRF_y - F_{ay} - W_{foot} &= 0 \\
 F_{ay} &= GRF_y - W_{foot} \\
 F_{ay} &= 685.41N
 \end{aligned} \tag{16}$$

$$\sum M_{COMx} = 0 \tag{17}$$

$$M_{ax} + GRF_z(COP_y - COM_{footy}) - GRF_y(COM_{footz} - COP_z) - F_{az}(COM_{footy}) = 0$$

$$M_{ax} = 2.28Nm$$

Knee:

$$\begin{aligned}
 \sum F_z &= 0 \\
 F_{anklez} - F_{kneez} &= 0 \\
 F_{kneez} &= F_{anklez} \\
 F_{kneez} &= 40.02N
 \end{aligned} \tag{18}$$

$$\begin{aligned}
 \sum F_y &= 0 \\
 F_{ay} - W_{shank} - F_{ky} &= 0 \\
 F_{ky} &= F_{ay} - W_{foot} \\
 F_{ay} &= 655.62N
 \end{aligned} \tag{19}$$

$$\sum M_{COMx} = 0 \tag{20}$$

$$M_{ax} + M_{kx} - F_{az}(L_{ay} - COM_{sy}) - F_{ay}(L_{az} - COM_{sz}) - F_{kz}(COM_{sy}) - F_{ky}(COM_{sz}) = 0$$

$$M_{kx} = 28.60Nm$$

Hip:

$$\begin{aligned}
 \sum F_z &= 0 \\
 F_{kz} - F_J \sin(\theta_{frocontact}) + F_{Mz} &= 0 \\
 F_J \sin(\theta_{frocontact}) &= F_{kz} - F_{Mz} \\
 F_J &= 1852.10N
 \end{aligned} \tag{21}$$

$$\sum F_y = 0$$

$$\begin{aligned}
F_{ky} - W_{thigh} - F_J \cos(\theta_{frocontact}) + F_{My} &= 0 \\
F_{My} &= -F_{ky} + W_{thigh} + F_J \cos(\theta_{frocontact}) \\
F_{My} &= 1071.70N
\end{aligned} \tag{22}$$

$$\sum M_J = 0 \tag{23}$$

$$M_{kx} + F_{ky}(L_{kz} - J_z) + F_{kz}(L_{ky} + J_y) + F_{Mz}(J_y) - F_{My}(J_z) + W_{thigh}(J_z - COM_{tz}) = 0$$

$$F_{Mz} = -854.86N$$

Sagittal Plane:

Ankle:

$$\begin{aligned}
\sum F_x &= 0 \\
GRF_x + F_{ax} &= 0 \\
F_{ax} &= -GRF_x \\
F_{ax} &= 82.88N
\end{aligned} \tag{24}$$

$$\sum M_{COMz} = 0 \tag{25}$$

$$M_{az} + GRF_x(COP_y - COM_{footy}) - F_{ax}(COM_{footy}) - GRF_y(COM_{fx} - COP_x) = 0$$

$$M_{anklesagittal} = 22.41Nm$$

Knee:

$$\begin{aligned}
 \sum F_x &= 0 \\
 F_{kx} - F_{ax} &= 0 \\
 F_{kx} &= F_{ax} \\
 F_{kx} &= 82.88N
 \end{aligned} \tag{26}$$

$$\sum M_{COMz} = 0 \tag{27}$$

$$-M_{az} + M_{kz} - F_{ax}(L_{ay} - COM_{sy}) - F_{ay}(L_{ax} - COM_{sx}) - F_{kx}(COM_{sy}) - F_{ky}(COM_{sx}) = 0$$

$$M_{kz} = 143.10Nm$$

Hip:

$$\begin{aligned}
 \sum F_x &= 0 \\
 F_J \cos(\theta_{sagcontact}) - F_{kx} - F_{Mx} &= 0 \\
 F_{Mx} &= F_J \cos(\theta_{sagcontact}) - F_{kx} \\
 F_{Mx} &= 837.45N
 \end{aligned} \tag{28}$$

C Inverse Dynamics Variable Definitions

Table A19: Variable names and values used in foot inverse dynamics analysis at 52% gait

Variable	Definition	Value
m_{foot}	Mass of foot	0.9469kg
a_{fx}	Linear acceleration of the COM of the foot in the x-direction	$7.83m/s^2$
GRF_x	Ground reaction force in x-direction	107.44N
R_{ax}	Reaction force at ankle in the x-direction	-96.73N
a_{fy}	Linear acceleration of the COM of the foot in the y-direction	$-2.39m/s^2$
GRF_y	Ground reaction force in the y-direction	729.77N
R_{ay}	Reaction force at ankle in the y-direction	720.5N
a_{fz}	Linear acceleration of the COM of the foot in the z-direction	$-0.64m/s^2$
GRF_z	Ground reaction force in the z-direction	47.33N
R_{az}	Reaction force at the ankle in the z-direction	50.18N
I_{fz}	Moment of inertia of the foot about the z-axis	$0.012m^2kg$
α_{fz}	Angular acceleration of the foot COM about the z-axis	$20.19rad/s^2$
Δx	Distance from COP to COM of foot in x-direction	-0.0314m
Δy	Distance from COP to COM of foot in y-direction	-0.0227m
ΔX	Distance from ankle to COM of foot in x-direction	0.0885m
ΔY	Distance from ankle to COM of foot in y-direction	0.0139m
M_{az}	Reaction moment at the ankle about the z-axis	37.3Nm
I_{fx}	Moment of inertia of the foot about the x-axis	$0.0043m^2kg$
α_{fx}	Angular acceleration of the COM of the foot about the x-axis	$-211.05rad/s^2$
M_{ax}	Reaction moment at the ankle about the x-axis	-2.83Nm

Table A20: Variable names and values used in shank inverse dynamics analysis at 52% gait

Variable	Definition	Value
m_{shank}	Mass of shank	3.04kg
a_{sx}	Linear acceleration of the COM of the shank in the x-direction	$7.59m/s^2$
R_{kx}	Reaction force at knee in the x-direction	-84.9N
a_{sy}	Linear acceleration of the COM of the shank in the y-direction	$-1.15m/s^2$
R_{ky}	Reaction force at knee in the y-direction	692.5N
a_{sz}	Linear acceleration of the COM of the shank in the z-direction	$-0.502m/s^2$
R_{kz}	Reaction force at the knee in the z-direction	58.65N
I_{sz}	Moment of inertia of the shank about the z-axis	$0.0408m^2kg$
α_{sz}	Angular acceleration of the foot COM about the z-axis	$10.91rad/s^2$
Δx	Distance from ankle to COM of shank in x-direction	0.0122m
Δy	Distance from ankle to COM of shank in y-direction	0.2173m
ΔX	Distance from knee to COM of shank in x-direction	0.0086m
ΔY	Distance from knee to COM of shank in y-direction	0.1659m
M_{az}	Reaction moment at the knee about the z-axis	15.99Nm
I_{fx}	Moment of inertia of the shank about the x-axis	$0.0408m^2kg$
α_{fx}	Angular acceleration of the COM of the foot about the x-axis	$-36.32rad/s^2$
Δz	Distance from the ankle to the COM of the knee in the z-direction	-0.0132m
ΔZ	Distance from the knee to the COM of the knee in the z-direction	0.0101m
M_{ax}	Reaction moment at the knee about the x-axis	3.69Nm

Table A21: Variable names and values used in thigh inverse dynamics analysis at 52% gait

Variable	Definition	Value
m_{thigh}	Mass of thigh	6.53kg
a_{ty}	Linear acceleration of the COM of the shank in the y-direction	$-0.131m/s^2$
β	Angle of muscle abductor muscle force in frontal plane	69.63°
F_{Jy}	Femoral head contact force in y-direction	1395.8N
F_M	Resultant abductor muscle force	815.25N

D Stress Calculations

The following stress calculations are shown for section C-C, as there is cement, bone and implant acting together, as well as contribution from both muscle and joint contact forces. The sample calculations are done for the static toe off case calculated in Section 11 since it had the highest forces. The equations show how to calculate the stress in the bone for the natural bone case ($\sigma_{cortNat}$) and the stress in the cortical bone after the implant is inserted ($\sigma_{cortImp}$). The same process is repeated to calculate the stress in the implant and the cement to determine safety factors. The results are in Table 15 to Table 17.

The location of the neutral axis, \hat{y} , is calculated for the natural bone by first finding the centroid of each material and then using the composite beam theory as seen in Equation 29.

$$\bar{y}_c = \frac{e * a^2}{1 - a^2} \quad (29)$$

$$\bar{y}_t = -0.0007$$

$$\hat{y}_{nat} = \frac{E_c * A_c * \bar{y}_c + E_t * A_t * \bar{y}_t}{E_c * A_c + E_t * A_t} \quad (30)$$

$$\hat{y}_{nat} = -0.00065$$

where E is the Youngs modulus of cortical or trabecular bone, e is the eccentricity of the trabecular bone in the cortical bone, a is the ratio of the cortical to trabecular bone areas, and A is the area of the cross section.

The \hat{y} value for the bone with the implant is given by

$$\bar{y}_c = \frac{e * (A_{imp} + A_{cem})}{A_{cort} - A_{imp} - A_{cem}} \quad (31)$$

$$y_{imp}^- = -0.0007 = y_{cem}^- \quad (32)$$

$$\hat{y} = \frac{E_c * A_c * \bar{y}_c + E_{cem} * A_{cem} * \bar{y}_{cem}^- + E_{imp} * A_{imp} * \bar{y}_{imp}^-}{E_c * A_c + E_{cem} * A_{cem} + E_{imp} * A_{imp}} \quad (33)$$

$$\hat{y}_{imp} = \frac{17 * 10^9 * 0.00035 * -0.0022 + 2 * 10^9 * 0.0001 * -0.007 + 100 * 10^9 * 0.00016 * -0.007}{17 * 10^9 * 0.00035 + 2 * 10^9 * 0.0001 + 100 * 10^9 * 0.00016}$$

$$\hat{y}_{imp} = -0.0011$$

The moment around the hip joint for the implant can be calculated using Equation 34 where θ is the angle of the cross section with respect to the horizontal axis. At this section, θ is equal to the Q-angle, which is 17° for this user, as seen in Figure 31.

$$M = F_{Jz}(D_{Jy} - \hat{y} * \sin \theta) + F_{Jy} * (D_{Jz} + \hat{y} * \cos \theta) + F_{Mz}(D_{My} - \hat{y} * \sin \theta) + F_{My} * (D_{Mz} + \hat{y} * \cos \theta) \quad (34)$$

$$M = 1007.2(0.09 + 0.001 * \sin 17) + 2106 * (0.021 - 0.001 * \cos 17) \\ + 736.6(0.045 + 0.001 * \sin 17) + 1922.9 * (0.033 - 0.001 * \cos 17)$$

$$M = 291 Nm$$

Where F_M is the muscle force and F_J is the joint contact force found from the inverse dynamic static analysis.

The axial force at the cross section is calculated in Equation 35

$$P = F_{JZ} * \sin \theta + F_{JY} * \cos \theta - F_{MZ} * \sin \theta + F_{MY} * \cos \theta \quad (35)$$

$$P = 1007.2 * \sin 17 + 2106 * \cos 17 - 736.6 * \sin 17 + 1922.9 * \cos 17 = -254N$$

The shear force at the cross section is calculated in Equation 36

$$V = F_{JZ} * \cos \theta + F_{JY} * \sin \theta - F_{MZ} * \cos \theta + F_{MY} * \sin \theta \quad (36)$$

$$V = 1007.2 * \cos 17 + 2106 * \sin 17 - 736.6 * \cos 17 + 1922.9 * \sin 17$$

$$V = -205.2N$$

The reaction moment at the cross section for the natural bone is calculated in the same way, by replacing the \hat{y} with the value for the natural bone.

The moments of inertia, I , about the neutral axis in the natural bone case for the cortical and trabecular bone are:

$$\hat{I}_c = \frac{\pi * D_c^4}{64} + \frac{\pi * D_c^2}{64} - \hat{I}_t \quad (37)$$

$$\hat{I}_t = \frac{\pi * D_t^4}{64} + \frac{\pi * D_t^2 * (\hat{y} - \bar{y}_t)^2}{64} \quad (38)$$

$$(39)$$

The moments of inertia about the neutral axis of the implant and cement are given in Equation 40 for the implant case.

$$\hat{I}_{imp} = \pi * r_{imp}^4 / 4 + \frac{b * h^3}{12} + A_{imp} * (y_{imp} - \hat{y})^2 \quad (40)$$

$$\hat{I}_{imp} = \pi * 0.005^4 / 4 + \frac{0.008 * 0.01^3}{12} + 0.00016 * (-0.0007 + 0.0011)^2$$

$$\hat{I_{imp}} = 3.54 * 10^{-9}m$$

$$\hat{I_{cem}} = \pi * r_{cem}^4 / 4 + \frac{b_{cem} * h_{cem}^3}{12} - I_{imp} + A_{cem} * (y_{cem}^- - \hat{y})^2 \quad (41)$$

$$\hat{I_{cem}} = \pi * 0.006^4 / 4 + 0.0052 * 0.006^3 / 12 - 3.54 * 10^{-9} + 0.00012 * (-0.007 + 0.0011)^2$$

$$\hat{I_{cem}} = 51.1 * 10^{-9}m$$

Using the Composite Beam Theory for the natural bone case for the cortical bone:

$$\begin{aligned} \sigma_{cortNatBM} &= \pm \frac{M * E_c * (r_c - \hat{y_{nat}})}{E_c * I_c + E_t * I_t} \\ \sigma_i &= \frac{-17.6 * 17 * 10^9 * (0.014 + 0.00065)}{17 * 10^9 + 1.07 * 10^{-9} + 11.4 * 10^9 * 15.8 * 10^{-9}} \\ &= -17.9 MPa \quad (42) \\ \sigma_s &= \frac{43.2 * 17 * 10^9 * (0.014 + 0.00065)}{17 * 10^9 + 1.07 * 10^{-9} + 11.4 * 10^9 * 15.8 * 10^{-9}} \\ &= -16.3 MPa \end{aligned}$$

Where r_c is the radius of the cortical bone.

Using the Composite Beam Theory for implant and bone case, for the cortical bone

the stress due to the bending moment is:

$$\begin{aligned}
\sigma_{cortImpBM} &= \frac{M * E_c * (r_c - \hat{y})}{E_c * I_c + E_{imp} * I_{imp} + E_{cem} * I_{cem}} \\
\sigma_i &= \frac{-25.3 * 17 * 10^9 * (0.014 - 0.0011)}{17 * 10^9 * 21.6 * 10^{-9} + 100 * 10^9 * 3.54 * 10^{-9} + 2 * 10^9 * 51.1 * 10^{-9}} \\
&= -29.8 MPa \\
\sigma_s &= \frac{-25.3 * 17 * 10^9 * (0.014 - 0.0011)}{17 * 10^9 * 21.6 * 10^{-9} + 100 * 10^9 * 3.54 * 10^{-9} + 2 * 10^9 * 51.1 * 10^{-9}} \\
&= -22.1 MPa
\end{aligned} \tag{43}$$

The stress due to the axial force is:

$$\begin{aligned}
\sigma_{cortNatP} &= \frac{P * E_c}{E_c * A_c + E_t * A_t} \\
&= \frac{-254.2 * 17 * 10^9}{17 * 10^9 * 0.00061 + 11.5 * 10^9 * 0.00043} \\
&= -0.265 MPa \\
\sigma_{cortImpP} &= \frac{P * E_c}{E_c * A_c + E_t * A_t} \\
&= \frac{-254.2 * 17 * 10^9}{17 * 10^9 * 0.00061 + 100 * 10^9 * 0.00016 + 2 * 10^9 * 0.00011} \\
&= -1.1 MPa
\end{aligned} \tag{44}$$

By adding the axial and bending moment stresses, the total stress can be obtained.

To determine the safety factors, this process is done for the implant and cement as well.

The bone with implant case is compared to the natural bone case to determine the percent of stress shielding from Equation 45

$$\text{StressShielding\%} = \frac{\sigma_{cortNat} - \sigma_{cortImp}}{\sigma_{cortNat}} \tag{45}$$

D.1 Hertz Theory

Table A22 indicates the material properties used for the Hertz Analysis.

Table A22: Material Properties for Hertz Analysis

CoCr Poisson's ratio (ν)	0.29 [152]
CoCr Youngs Modulus (E)	210GPa [152]
CoCr Ultimate Strength (S_u)	1449 MPa [153]
XLPE Poisson's ratio (ν)	0.4 [154]
XLPE Youngs Modulus (E)	0.67GPa [154]
XLPE Ultimate Strength (S_u)	52MPa [155]

$$\begin{aligned}
 C_m &= \frac{1 - \nu_{PE}^2}{E_{PE}} + \frac{1 - \nu_{CoCr}^2}{E_{CoCr}} \\
 C_m &= \frac{1 - 0.4^2}{0/67 * 10^9} + \frac{1 - 0.29^2}{210 * 10^9} = 1.6 * 10^{-9} \\
 C_G &= \frac{D_{cup} * D_{ball}}{D_{cup} + D_{ball}} \\
 C_G &= \frac{0.032 * 0.03202}{0.032 + 0.03202} = 0.016 \\
 a &= 0.721 * (PC_M C_G)^{\frac{1}{3}} \\
 a &= 0.721 * (1650.2 * 1.6 * 10^{-9} * 0.016)^{\frac{1}{3}} = 0.0023 \\
 P_{max} &= \frac{1.5P}{\pi a^2} \\
 P_{max} &= \frac{1.5 * 1650.2}{\pi * 0.0023^2} = 146.4 MPa
 \end{aligned} \tag{46}$$

The alternating σ_a and mean stress σ_m are then calculated in Equation 47.

$$\begin{aligned}
 \sigma_m &= \frac{\sigma_{max} + \sigma_{min}}{2} = 148.87 MPa \\
 \sigma_a &= \frac{\sigma_{max} - \sigma_{min}}{2} = 72.67 MPa
 \end{aligned} \tag{47}$$

The safety factor is then found in Equation 48

$$\frac{1}{SF} = \frac{\sigma_m}{S_u} + \frac{\sigma_a}{S_u} \quad (48)$$

For CoCr:

$$SF = \left(\frac{148.9}{1449} + \frac{72.62}{1449} \right)^{-1} = 6.54 \quad (49)$$

For XLPE:

$$SF = \left(\frac{148.9}{52} + \frac{72.62}{52} \right)^{-1} = 4.26 \quad (50)$$

E Muscle Force Angle and Location

It is difficult to find values of muscle force location and angle throughout gait. Therefore information from Khasawneh et al., Henderson et al. and Winters anthropometric data were used to determine the location and angle at key locations during gait [95, 156, 157]. The exact angle of the muscle force during standing could not be found but based on various biomechanics textbook examples seen it is approximately 71°, see Figure E.34.



Figure E.34: Muscle and femoral head angles

Using the moment arm data from Henderson et al. and the angles above the length

from the muscle connection point to the joint contact was determined as in Figure E.35.

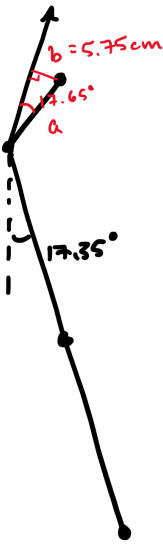


Figure E.35: Moment arm and muscle attachment dimensions

$$\sin(17.65) = \left(\frac{b}{a}\right) \quad (51)$$

$$a = 18.96\text{cm} \quad (52)$$

It can be seen that the value for a appears to be large, this is likely due to the source geometrical data for each paper which may have different data sources. Using the hip angle at loading response (18°), the muscle attachment and angle can be determined, see Figure E.36.

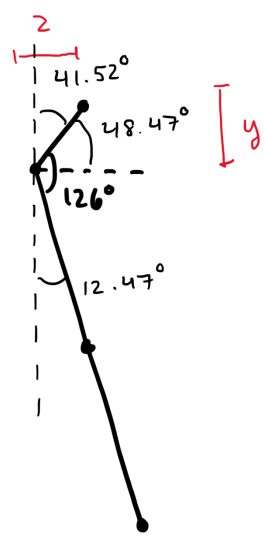


Figure E.36: Location and angle of the muscle at loading response

Using trigonometry y and z can be determined.